Microwave-assisted hydrothermal fabrication of hierarchical-stacked mesoporous decavanadate-intercalated ZnAl nanolayered double hydroxide to exterminate different developmental stages of *Trichinella spiralis* and *Schistosoma mansoni in-vitro*

Atef S. Darwish [a,*], Soheir S. Mahmoud [b], Fatma E.A. Bayaumy [c]

[a] Department of Chemistry, Faculty of Science, Ain Shams University, 11566, Cairo, Egypt
[b] Schistosome Biological Materials Supply Program, Theodor Bilharz Research Institute, Giza, Egypt
[c] Zoology Department, Faculty of Women for Arts, Science and Education, Ain Shams University, Cairo, Egypt

ABSTRACT

Hierarchically stacked mesoporous zinc-aluminium nanolayered-double-hydroxide intercalated with decavanadate (ZnAl-LDH-$V_{10}O_{28}$) is constructed using anion-exchange process via microwave-hydrothermal treatment. Physicochemical properties of ZnAl-LDH-$V_{10}O_{28}$ are characterized in detail. Decavanadate anions are intimately interacted with ZnAl-LDH nanosheets, generating highly ordered architecture of well-dimensioned stacking blocks of brucite-like nanolayers (~8 nm). Such hierarchy improves surface-porosity and electrical-impedivity of ZnAl-LDH-$V_{10}O_{28}$ with declining its zeta-potential (ζ_{av} = 8.8 mV). *In-vitro* treatment of various developmental-stages of *Trichinella spiralis* and *Schistosoma mansoni* by ZnAl-LDH-$V_{10}O_{28}$ is recognized using parasitological and morphological (SEM/TEM) analyses. ZnAl-LDH-$V_{10}O_{28}$ exterminates muscle-larvae and adult-worms of *Trichinella spiralis,* and juvenile and adult *Schistosoma mansoni*, yielding near 100% mortality with rates achieving 5%/h within about 17 h of incubation. This parasiticidal behavior results from the symphony of biological activity gathering decavanadate and LDH-nanosheets. Indeed, ZnAl-LDH-$V_{10}O_{28}$ nanohybrid sample, as a promissory biocide for killing food-borne/waterborne parasites, becomes a futuristic research hotspot for studying its *in-vivo* bioactivity and impact-effectiveness on parasite molecular biology.

1. Introduction

Layered double hydroxides (LDH) are a pioneering class of synthetic inorganic two-dimensional lamellar materials that exhibit positively charged layers resembling brucite with intercalated anions occupying the interlayer spacing to maintain charge neutrality [1–3]. Interlamellar spacings in the nitrate forms of LDH are highlighted as promising candidate to originate "galleries" in which NO_3^- ions are suggested to be efficiently released and exchanged by other "guest" polyanions [4,5]. Besides, owing of nitrate forms of LDH to various structural modes and flexible chemical composition, unique memory effect, advanced surface characteristics, and high

---

stability, strongly devotes their widespread usage in fundamental research and various fields of industrial and environmental purposes [3,5,6]. Accordingly, these LDH materials are supposed to be attractive for application in heterogenous catalysis, photocatalysis, and electrocatalysis [6–10], energy storage and conversion [11–13], corrosion inhibition of alloys [14,15], flame retardancy [1,16], and water purification [2,3,9]. Moreover, the acquisition of NO_3^- containing LDH materials to advanced anion exchange capacity kindly recommends the interlamellar spaces as attractive hosts for storage and controllable delivery of numerous organic and inorganic anions [1,17–19]. Unfortunately, as the nitrate form of LDH comprises domains of parallelly compacted hydroxide layers [18,20], most of brucite-type layers seriously suffer degeneration of surface nature and pore structure [18,19,21]. To tackle this drawback, encouraging option is proposed in literature based on replacement of NO_3^- ions with polyoxometalate anions, which are intercalated into the interlamellar galleries of LDH to construct a hierarchical architecture of LDH layers [4,20,22,23]. By this way, the porous structure of LDH materials is significantly enhanced and their interlamellar spacings appear to gain potential importance as effective "hosting system", and thus further improves the performance of brucite-like layers in the fields of heterogeneous catalysis and photocatalysis, and corrosion inhibitors [20,22,24–26].

Decavanadate $[V_{10}O_{28}]^{6-}$, as a representative polyoxometalate, is one of the most important intercalating agents that gains substantial attention in the industrial field due to several reasons, including, (i) the proficient contribution of peroxo-V centres, V–O–V bonds as well as V^{5+}/V^{4+} redox pairs in different catalytic processes, e.g., epoxidation, alkoxylation, oxidative dehydrogenation, etc. [24,27,28], and (ii) the pivotal role of $V_{10}O_{28}^{6-}$ in protecting steel from corrosion by aggressive chloride ions through increasing the impedance of LDH structure, and favouring the anion exchange reaction where the brucite-like layers are susceptible to trap Cl^- ions synchronously with releasing the interlayered decavanadate anions [29–31].

Among all the mixed metal oxides reported in literature, zinc aluminium layered double hydroxide (ZnAl-LDH) stands as a candidate for efficient intercalation of decavanadate species because of its tendency to display robust interlamellar zones that are intimately attached to $V_{10}O_{28}^{6-}$ anions via electrostatic and hydrogen-bonding interactions [2,17,24]. Such combination plausibly imparts extra stability to the formed decavanadate intercalated LDH system with restricted releasing of the intercalated molecules [17, 26]. Nevertheless, tightly packed stacks of randomly arranged microporous brucite-like layers are regrettably formed by being intercalated with decavanadate ions using conventional approaches like co-precipitation, microwave, and hydrothermal methods [18, 19,26]. Unfortunately, inventing new synthetic routes to enhance the physicochemical feature of decavanadate intercalated ZnAl-LDH system are still lacking in literature. To our knowledge, there have been no documented reports in the literature regarding the fabrication of hierarchically stacked and highly ordered decavanadate intercalated ZnAl-LDH sheets of mesoporous feature using microwave-hydrothermal treatment.

During the last few years, the medicinal chemistry of ZnAl-LDH material and vanadium-based species, in particular, decavanadate ion, have been exponentially increased. ZnAl-LDH material is widely used in pharmaceutical industry as intelligent excipient for drug delivery purposes, as it confers an interlayer gallery space which enables the intercalation of various therapeutic agents, e.g., anti-cancer [32], antiviral [33], antineoplastic and cosmetic agents [34,35], and releases them distinctly to the target site, thereby reducing the frequency of drug administration and its adverse effect as well [36]. Moreover, owing of ZnAl-LDH to high biocompatibility, low toxicity, and cell adhesion and proliferation, render it to be promisingly used as bone implants, and anti-inflammatory as well as antimicrobial agents [36–38]. Alternatively, decavanadate ions are suggested to be a promissory agent for cancer treatment [39–41] due to its toxicological effect against the cancer cells and tendency to bind with the biological receptors, proteins, and enzymes in the diseased cells [42,43]. To the best of our knowledge, the bioavailability of the combined system comprising the two merits above-mentioned ZnAl-LDH and $V_{10}O_{28}^{6-}$ species has not yet been probed in literature.

In spite of looking forward to overcoming the global impact of communicable diseases, parasitic infections are still worldwide problems that cause potential public health hazards [44]. Severe infections caused by *Trichinella spiralis* and *Schistosoma mansoni* are worldwide distributed, covering the developed, developing, and underdeveloped countries, where not only high temperature and humidity prevail, but also poor health status are common [45,46]. Trichinellosis is a foodborne illness caused by the consumption of raw or undercooked meat, which contains viable infective *Trichinella larvae* [47,48]. Such parasitic disease affects about 11 million individuals around the world [48]. The entire life cycle of *Trichinella spiralis* (*T. spiralis*) occurs within a single host. Upon ingestion of the infected meat, the larvae migrate to the stomach and undergo maturation into adult worms [48]. The newly born larvae emerge from the fertilized female, detach from the intestinal wall, and ultimately enter the bloodstream [48]. Only the larvae that successfully reach the striated muscles are able to survive by (i) converting the infected muscle cells into nurse cells [47,48], and (ii) being encapsulated via setting-up a hard and thick outer shell of collagen fibre [48,49]. Such defence strategies in *T. spiralis* enthuse survival of muscle larvae for several years or even throughout the entire life of the host, leading to extreme destruction of muscle cells, respiratory problems, kidney failure, depression of pulse and blood pressure, heart attacks, nervous disorders, and in many cases, fatality [46,48]. Schistosomiasis is a waterborne illness that impacts approximately 200 million individuals worldwide [50]. The infective stage cercariae of *Schistosoma mansoni* (*S. mansoni*), hosted by freshwater snails, actively pierce the human skin, enter blood vessels, and migrate to venules that drain into the large intestine [51]. Based on this migration profile, the juvenile as well as the adult worm stages are developed [51,52]. Human infection with any of the developmental stages of *S. mansoni* rarely causes death, but the organs are progressively damaged displaying gastrointestinal bleeding, haematuria (blood in urine), sepsis, extreme anaemia, and can potentially lead to liver and bladder cancer [52,53]. Recently, Elbaz and Esmat postulate that infected people by *S. mansoni* adult worms are significantly susceptible to deadly infectious diseases like HIV/AIDS [54].

Up to now, vaccines for trichinellosis and schistosomiasis are not yet available, as treating trichinellosis is hanged by using benzimidazole derivatives drug (albendazole and mebendazole), while primary treatment for schistosomiasis principally relies on a single medication, praziquantel [47,52]. The extensive utilization of these antiparasitic drugs, coupled with reports of new trichinella and schistosome strains exhibiting diminished responsiveness to these drugs [47,50], may strongly raises alarming concerns about the

potential development of drug resistance. In addition, none of these familiar drugs are proficient to damage the encapsulated *T. spiralis* larvae or the juvenile *S. mansoni* worms during the early stages of infection because of their low bioavailability [49,55]. Besides, most of these drugs pose risks for pregnant women and children under the age of two [56]. Hence, looking for prudent alternatives to the common antiparasitic drugs used to treat the invasive stages in the life cycle of *T. spiralis* and *S. mansoni* has received mounting attention over the recent few years [46,51,57].

The current work, as a first study of its kind in literature, aims to build-up hierarchically stacked and highly ordered mesoporous ZnAl layered double hydroxide nanosheets via being intercalated with decavanadate anions using microwave-hydrothermal method, and explore their parasiticidal *in vitro* activity against different developmental stages of *T. spiralis* and *S. mansoni*.

2. Materials and methods

2.1. Reagents and chemicals

Zinc (II) nitrate hexahydrate ($Zn(NO_3)_2 \cdot 6H_2O$), aluminium (III) nitrate heptahydrate ($Al(NO_3)_3 \cdot 9H_2O$), and sodium metavanadate ($NaVO_3$) were obtained from Merck (Darmstadt, Germany). Potassium hydroxide (KOH), potassium nitrate (KNO_3), and praziquantel (PZQ), as a reference anti-schistosomal drug, were supplied from Sigma-Aldrich Co. (St. Luis, MO, USA). Albendazole (ALB), as a reference anti-Trichinella drug, was procured from Amoun Pharmaceutical Industries Company, El Obour city, Egypt. Nitric acid (HNO_3, 65% purity) was purchased from PROLABO Chemical Reagents Co. Ltd. All remaining chemicals used were of analytical grade.

2.2. Parasite material

The *T. spiralis* muscle larvae and adult worms were supplied by Schistosome Biological Supply Centre (SBSC) at Theodor Bilharz Research Institute (TBRI, Giza, Egypt), following the protocols described elsewhere [47,58–60]. Both *T. spiralis* muscle larvae and adult worms were thoroughly washed multiple times with phosphate buffer saline (PBS) and subsequently counted under a light microscope at 40× magnification, following the methodology described in previous study [60]. The *S. mansoni* juvenile and adult worms were also supplied from SBSC, TBRI, Giza, Egypt, following the method discussed elsewhere [50]. These worms were washed and numbered adopting the same procedure used for *T. spiralis*.

2.3. Synthesis of nitrate containing zinc aluminium layered double hydroxide (ZnAl-LDH-NO₃)

Preparation of parent ZnAl-LDH-NO₃ material was carried out with a nominal Zn/Al molar ratio of 2:1 using co-precipitation method [61]. Such proportion was chosen to insure designing of highly stable layered material of pronounced bioactive nature [33,61]. A solution of KOH was gently added to a homogeneous mixture consisting of zinc nitrate, aluminium nitrate, and potassium nitrate. The produced suspension was refluxed overnight. The resulting residue was collected, washed, dried, and finally ground to fine powder. More details about the synthesis of ZnAl-LDH-NO₃ sample are further described in Text S1 in supporting information.

2.4. Microwave irradiation-activated hydrothermal synthesis of hierarchical stacked mesoporous decavanadate intercalated zinc aluminium layered double hydroxide (ZnAl-LDH-V₁₀O₂₈)

The decavanadate intercalated ZnAl layered double hydroxide sample was prepared through ion exchange from the parent ZnAl-LDH-NO₃, using a modified version of the method discussed in previous work [62]. After 24 h rehydration of 1 g of parent ZnAl-LDH-NO₃ sample in 100 ml deionized water at ambient temperature in an ultrasonic bath with N₂ purging, the pH of the resulting suspension was regulated to a range of 4.5–5.5 using a 2 M HNO₃ solution.

In a separate container, a proper amount of NaVO₃ (8.85 mmol, 1.079 g) was dissolved in 70 ml of hot deionized water and acidified to a pH of 4.5, thus yielding an orange solution of decavanadate species with a concentration of 12,104 μg/ml [25]. The vanadium content in the provided orange solution was determined using inductively coupled plasma atomic spectroscopy method (ICP-AES). No discrepancies were observed between the measured and the expected theoretical values. The resulting orange solution of decavanadate was stored under vacuum at 4 °C and nominated by "V₁₀O₂₈".

A proper amount of the so-synthesized decavanadate solution was gently added to the suspension of parent ZnAl-LDH-NO₃ over *ca.* 20 min at ambient temperature under N₂ purging, while the pH was kept at 4.5. The added amount of decavanadate solution was chosen to yield an atomic percent vanadium of about 50% greater than that of Al^{3+} cations in the crystal structure of ZnAl-LDH-V₁₀O₂₈. This resulted in a vanadium fraction relative to the other metal atomic ratios (V/(Zn + Al)) of 0.5376. Such proportionality of $[V_{10}O_{28}]^{6-}$ in the interlayer spacing of LDH was interpreted in previous reports [28,63], where the amount of decavanadate anions were designed to fully neutralize the positive charge of the brucite-type layer, which originated from the partial substitution of divalent cations (Zn^{2+}) with trivalent cations (Al^{3+}) [28]. The obtained reaction mixture was transferred to a 250-ml Teflon autoclave, which was filled to approximately 70% capacity. The autoclave was then placed in a microwave oven (CEM MARS-240/50) operating at a frequency of 2.45 GHz and a maximum power of 650 W. This process generated a pressure within the autoclave reaching about 0.11 MPa. The microwave-assisted hydrothermal route was conducted at 120 °C for 6 h, with a heating rate of 10 °C/min. Subsequently, the autoclave was allowed to cool down naturally, and the obtained precipitate was then centrifuged, washed, and dried following a protocol relevant to that described in Sec. *2.3*. The resultant yellow-orange powder was named "ZnAl-LDH-V₁₀O₂₈". For comparison purposes, the hydrothermal treatment was performed individually for synthesis of decavanadate intercalated ZnAl layered double

hydroxide following the formerly defined reaction conditions, and the finally obtained colored powder was labelled by "ZnAl (H)-LDH-$V_{10}O_{28}$".

2.5. Characterization of samples under investigation

Structural characteristics of the parent ZnAl-LDH-NO_3, and ZnAl-LDH-$V_{10}O_{28}$ and ZnAl (H)-LDH-$V_{10}O_{28}$ hybrid samples were performed using different analytical techniques. X-ray diffraction patterns were recorded on a Philips PW3710-BASED diffractometer equipped with Ni-filtered CuKα radiation (λ = 1.5418 Å). The instrument was operated at 40 kV and 50 mA. The scanning range of 2Θ was set from 5° to 80°, with a scanning rate of 1° per minute. The interlayer spacings (d, Å) of the brucite-type structure in the under investigated samples were recognized using Bragg's method of crystal analysis [64]. Fourier transform infrared spectra (FTIR) were carried out using ATi Mattson, WI, 53,717 model Genesis spectrometer (USA) with a resolution of 2 cm^{-1}. Raman spectra were acquired using a Jobin-Yvon LabRam HR800 instrument, with 532 nm excitation by Nd-YAG laser source and 0.23 mW laser power of a wavenumber accuracy of 2 cm^{-1}. Additionally, X-ray photoelectron spectroscopy (XPS) analysis was conducted using an ESCA Lab 250Xi instrument from Thermo Scientific to recognize the chemical and electronic states of Zn, Al, V, and O elements in the under-studied samples, following previously reported protocol [64]. An Al Kα X-ray source with a photon energy (hν) of 1486.6 eV was utilized at 15 kV and 25 W. The incident beam diameter as well as the constant pass energy were set to 200 μm and 58.7 eV, respectively, throughout the analysis.

The morphology of the parent ZnAl-LDH-NO_3 and ZnAl-LDH-$V_{10}O_{28}$ samples was examined using a scanning electron microscope (SEM, JEOL-JSM T2000) coupled with a JEOL-T20-CSI model camera. The SEM instrument used in this study was equipped with an energy-dispersive X-ray detection system (Oxford D6679 EDX detector). The measurements were performed under high-vacuum mode with 20 kV acceleration voltage to estimate the elemental composition of the samples under study in terms of weight percent (wt.%) and atomic percent (at.wt.%). High-resolution transmission electron microscope (HRTEM, JEOL-2100) operating at 200 kV with a resolution of 0.14 nm was utilized for morphological assessment of the understudied samples. The textural properties of these samples were demonstrated by analysing the N_2 adsorption-desorption isotherms at −196 °C using a Quantachrome TouchWin v1.2 device. Prior to analysis, the samples were subjected to vacuum outgassing at 120 °C for 3 h. The apparent surface areas (S, m^2 g^{-1}) were determined using the multi-point Brunauer-Emmer-Teller (BET) method over a P/P_o range of 0.025–0.30 [65]. The total pore volumes (V_P, ml g^{-1}) were calculated based on the amount of N_2 adsorbed at 0.99 P/P_o. The most abundant hydraulic pore diameters ($\bar{r}_h$, Å) were evaluated from the pore size distribution (PSD) curves by the aid of Barrett-Joyner-Halenda (BJH) model [66]. The average pore radii (r_p, Å) were calculated using Eq. (1), assuming a cylindrical or slit-shaped pore model [66].

$$r_P (\text{Å}) = (2V_P / S) \text{ x } 10^4 \tag{1}$$

Zeta-potential distribution curves, average zeta-potential values (ζ_{av}, mV), particle size distribution profiles (hydrodynamic diameter) and conductivity (mS/cm) were analyzed for both the parent ZnAl-LDH-NO_3 and the ZnAl-LDH-$V_{10}O_{28}$ hybrid sample using dynamic light scattering (DLS) technique. The measurements were conducted with the assistance of a Malvern zeta sizer-Nano ZS90 (United Kingdom) instrument, following the methodology discussed elsewhere [64]. The electrical impedance (Z) data of samples under investigation were recorded at ambient temperature using an LCR Meter IM3536 analyzer, where the measurements were performed over a range of alternating current (ac) frequencies from 10 Hz to 7 MHz.

2.6. Cell viability and imaging examination of ZnAl-LDH-$V_{10}O_{28}$ hybrid sample

The African green monkey kidney cell line known as Vero was obtained from the American Type Culture Collection, Manassas, VA, USA. The Vero cell line was cultured using Dulbecco's Modified Eagle's Medium (DMEM-Sigma) supplemented with 10% fetal bovine serum (Sigma) and 1 × antibiotic and antimycotic solution (Gibco) [46]. Vero cells were maintained in 96-well plates (Sigma-Aldrich) at a density of 10^4 cells/well and kept in a humidified incubator at 37 °C. Following an initial 24-h incubation period, varying concentrations of ZnAl-LDH-$V_{10}O_{28}$ hybrid material (ranging from 25 to 350 μg/ml) were individually dispersed in deionized water and added to each well. The cells were then further incubated for an additional 24 h. Cells incubated alone with DMEM medium were managed as a control. Afterwards, the medium in each well was rinsed with Hank's balanced salt solution (HPSS) and replaced with fresh medium (100 μl/well) for a 24-h period. To ensure accuracy, each experiment was repeated five times. The cell viability of the as-prepared sample was assessed using the Tetrazolium (MTT) cell proliferation assay kit supplied by Duchefa Biochemie, Netherlands. The optical densities (OD) were measured at 570 nm using infinite® M200 PRO multi-mode microplate reader (Tecan, Switzerland). The cell viability (%) was given by the following equation [46],

$$\text{Cell viability } (\%) = (OD_T / OD_C) \text{ x } 100 \tag{2}$$

Where OD_T and OD_C ascribed to the mean optical densities of the treated cells and the untreated control samples, respectively.

Moreover, after the aforementioned 48-h incubation period, the morphology of the Vero cells treated with varying concentrations of ZnAl-LDH-$V_{10}O_{28}$ hybrid material was examined using an inverted microscope (Eclipse Ti-E, Nikon, Japan).

2.7. Parasiticidal activity in vitro of ZnAl-LDH-V₁₀O₂₈ against muscle larvae and adult worms of T. spiralis

2.7.1. Experimental design and treatment conditions

The *in-vitro* anti-trichinella assay was achieved on muscle larvae (systemic phase) and adult worms (intestinal phase) following the protocol described in previous reports [47]. The culture medium used in this study was Roswell Park Memorial Institute medium (RPMI 1640) supplemented with the following components: gentamicin (160 g/ml), streptomycin (300 g/ml), penicillin (300 IU/ml), L-glutamine and fetal bovine serum (20% v/v). For this study, a sterile 24-well microtiter plates (Corning) were fed by *T. spiralis* muscle larvae, using 50 muscle larvae in 1 ml of culture medium per well. These larvae were then co-cultured with different concentrations of ZnAl-LDH-V₁₀O₂₈ suspension in the range 25–200 μg/ml at pH ~6.5. Alternatively, another 24-well culture plates were conducted by *T. spiralis* adult worms in presence of the same defined concentrations of ZnAl-LDH-V₁₀O₂₈ suspension at pH ~6.5, where each well was provided by 1 ml culture medium containing 50 adult worms. All of the plates were securely sealed and subsequently incubated at 37 °C in an atmosphere enriched with 5% CO_2 for different time intervals (6–36 h). Also, control experiments including sole exposure of 50 *T. spiralis* muscle larvae and/or adult worms to 1 ml culture medium were executed, following the above-described incubation procedure. For comparison purposes, reference drug ALB was submitted to parasitic culture media at a concentration of 30 μg/ml, i.e., ALB was dissolved in 1% v/v dimethyl sulphoxide before being incubated in the referenced well [47,51]. Each experiment was conducted three times, and the reported results are the average values from these repetitions.

2.7.2. In vitro evaluation of anti-Trichinella spiralis activity

At the end of incubation periods, in all the examined wells, the dead and living parasites, whether *T. spiralis* ML or adult worms, were enumerated using an inverted microscope of 100-fold magnification (Nikon CK40). The parasite death was determined when no motor activity was observed in the worm body for a minimum duration of 2 min. The % mortality for both *T. spiralis* ML and adult worms was expressed by Eq. (3).

$$\text{Mortality (M, \%)} = (M_{Test} / M_{Control}) \times 100 \tag{3}$$

Where M_{Test} represented the number of dead parasites (whether larvae or adult worms) in the treated wells, and $M_{Control}$ referred to the number of parasites in the control untreated well. To generalize the biological activity of ZnAl-LDH-V₁₀O₂₈ hybrid material, its parasiticidal results were compared with those obtained by treating *T. spiralis* ML and adult worms with the reference ALB drug. A comparative approach could be achieved by further studying the *in vitro* biological activity of ZnAl-LDH-NO₃ as well as orange decavanadate solution (V₁₀O₂₈) against *T. spiralis* muscle larvae and adult worms using the found highly efficient parasiticidal concentration of ZnAl-LDH-V₁₀O₂₈.

Moreover, deterioration in the morphological nature of *T. spiralis* ML and adult worms after being exposed to the found highly efficient concentration of ZnAl-LDH-V₁₀O₂₈, namely, 150 μg/ml, for 24-h incubation period was assessed using a scanning electron microscope (SEM, Inspect S, FEI Company, Holland), following a protocol described elsewhere [46,47]. Furthermore, high-resolution transmission electron microscope (HR-TEM, JEOL, JEM-1010, USA) was employed to identify any tissue damage within the bodies of the treated *T. spiralis* adult worms. For the purpose of comparison, after an incubation time of 24 h, the ultrastructure of the control untreated *T. spiralis* ML and adult worms, and their morphological changes when treated with reference ALB drug were also investigated.

2.8. In vitro bioactivity of ZnAl-ldh-v10o₂₈ against juvenile and adult worms of S. mansoni

2.8.1. Experimental in-vitro study design

The *in-vitro* anti-schistosomal assay was conducted on both juvenile and adult worms following the method outlined in previously published work [51]. The used culture medium was RPMI 1640, being relevant to that submitted in the *in-vitro* anti-Trichinella assay. The freshly recovered *S. mansoni* juvenile worms were placed in 24-well culture plates (Costar), with 10 worms suspended in 2 ml of culture medium per well. These worms were then co-cultured with various concentrations of ZnAl-LDH-V₁₀O₂₈, ranging from 25 to 200 μg/ml, at pH ~6.5. Also, the retrieved viable *S. mansoni* adult worms were collected and incubated in separate 24-well culture plates in presence of ZnAl-LDH-V₁₀O₂₈, where the number of *S. mansoni* adult worms in each well as well as the concentration range of the examined hybrid material and the pH of the obtained suspensions were analogue to those used in the treatment of *S. mansoni* juvenile worms. For comparison, a reference PZQ drug was suspended in 2 ml parasitic culture medium to form a concentration of 5 μg/ml and used in the treatment of either juvenile or adult worms of *S. mansoni*. Moreover, the control untreated experiments based on alone exposure of parasite (juvenile or adult worms) to 2 ml culture medium were carried out, adopting the same defined number of worms as mentioned above. The incubation conditions in all cultures were kept like those described in Sec. *2.7.1*. Each experiment was carried out three times.

2.8.2. Anti-schistosomal in-vitro evaluation

By the end of the incubation time intervals (6–36 h), the amount of dead and living *S. mansoni* (juvenile and/or adult worms) were counted using an inverted microscope, following the above-described procedure in Sec. *2.7.2*. Also, the % mortality of *S. mansoni* juvenile and adult worms were calculated according to Eq. (3). But here, the M_{Test} and $M_{Control}$ in that equation were denoted to the number of dead juvenile or adult *S. mansoni* worms, and the number of viable juvenile or adult *S. mansoni* worms in the control untreated well, respectively. Moreover, the parasiticidal activity of ZnAl-LDH-V₁₀O₂₈ hybrid material was compared with that of

reference PZQ drug against the juvenile and adult worms of *S. mansoni*. For further comparison, the *in vitro* biological behavior of the found highly efficient concentration of ZnAl-LDH-$V_{10}O_{28}$ hybrid sample (namely, 150 µg/ml) against *S. mansoni* juvenile and adult worms were compared with those extracted from using $V_{10}O_{28}$ orange solution as well as parent ZnAl-LDH-NO_3, adopting the same concentration for study.

Degeneration in the morphology of *S. mansoni* juvenile and adult worms after exposure to the found highly efficient concentration of ZnAl-LDH-$V_{10}O_{28}$, namely, 150 µg/ml, for 24 h incubation time was studied using SEM and TEM analyses, as previously described in Sec. *2.7.2*. For comparison, the morphological feature of the control untreated *S. mansoni* juvenile and adult worms alongside the
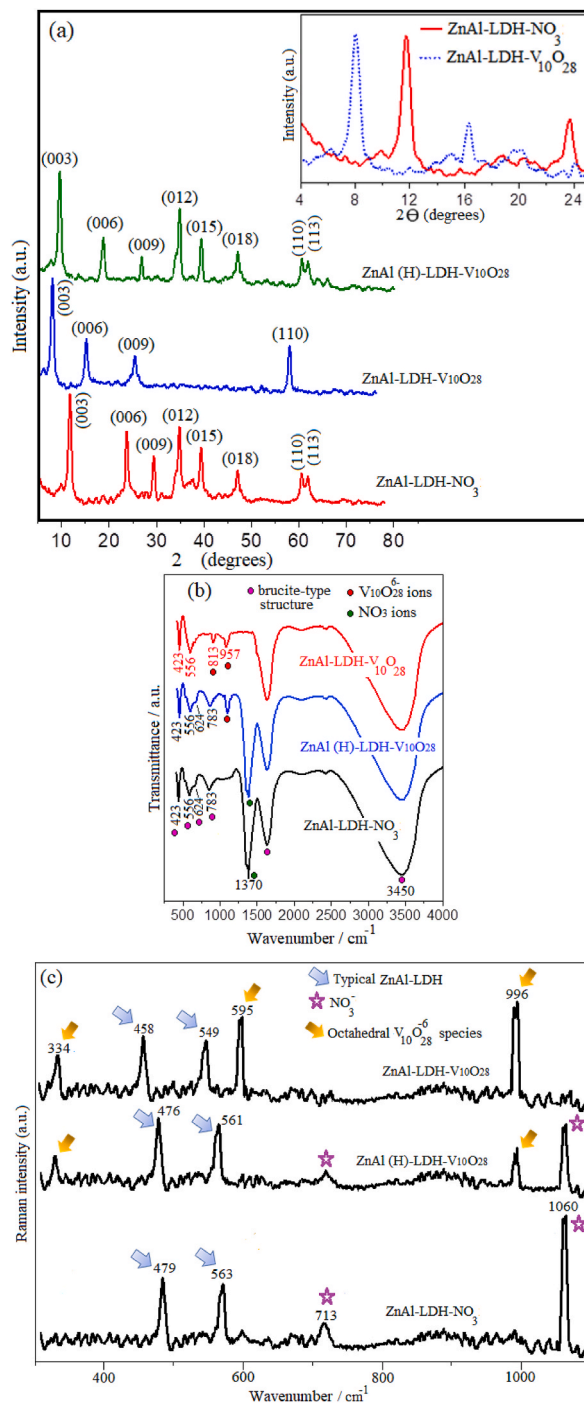
Fig. 1. XRD patterns (a) of samples under study (the inset image shows enlarged view of the XRD diffractograms of parent ZnAl-LDH-NO_3 and ZnAl-LDH-$V_{10}O_{28}$ nanohybrid material), and FT-IR spectra (b) as well as Raman patterns (c) of samples under investigation.

treated juvenile and adult worms with reference PZQ drug were further evaluated.

2.9. Statistical analysis

The parasitological data obtained in this study were calculated as the mean $\pm$ standard deviation (Mean $\pm$ SD) using Microsoft Excel and Origin 8© software.

3. Results and discussions

3.1. XRD analysis

The X-ray diffraction measurement is performed to elucidate the impact of the anion exchange on the structure of zinc aluminium layered double hydroxide. The XRD patterns of parent ZnAl-LDH-NO$_3$, ZnAl-LDH-V$_{10}$O$_{28}$ and ZnAl (H)-LDH-V$_{10}$O$_{28}$ are shown in Fig. 1 (a). The XRD profile of ZnAl-LDH-NO$_3$ (Fig. 1 a) represents the aculeate diffraction peaks of (003), (006), and (009) basal planes with d-spacings equivalent to 7.171 Å, 3.619 Å, and 2.437 Å, respectively, matching a standard pattern (JCPDS 48–1023) [67,68]. These basal spacings likely follow the relation $d_{003} \approx 2d_{006}$ pointing most probable to exhibition of ZnAl-LDH-NO$_3$ to a brucite-like structure. The lattice parameter c, which is ascribed to the stacking direction (axis c), is evaluated from the relation $c = 3d_{003}$ to yield a value of ~2.15 nm. Other peaks at relatively high 2θ values can be related to the non-basal reflections of (012), (015), (018), and (113) planes (Fig. 1 a), accommodating abundant presence of defect surfaces in the lamellar structure of ZnAl-LDH-NO$_3$ sample [69]. These results are in consistent with previously published works [67,70]. Also, the average crystallite size of the parent ZnAl-LDH-NO$_3$ sample is estimated by applying the Debye-Scherrer equation to the XRD characteristic peaks of the LDH structure, including (003), (006), and (009) crystal planes [46]. The domain crystallite size of brucite-like layers is found to be ~32 nm, indicating presence of relatively large sized ZnAl nanolayered double hydroxide.

For ZnAl-LDH-V$_{10}$O$_{28}$ hybrid system, the XRD diffractogram (Fig. 1 a) shows intactness of the well-defined crystallite brucite-like structure accompanied by notable agreement between the d-spacing values belonging to the successive reflections by basal planes, i.e., $d_{003} = 2d_{006} = 3d_{009}$. Furthermore, the reflections related to the non-basal planes for ZnAl-LDH-V$_{10}$O$_{28}$ hybrid sample disappear disseminating absence of surface defects and presence of a well-formed crystalline brucite-type structure. By comparing the XRD pattern of ZnAl-LDH-V$_{10}$O$_{28}$ with that of the parent ZnAl-LDH-NO$_3$, the main characteristic diffraction peaks are remarkably shifted to lower angles (viz., from 11.89° to 8.03° and from 23.69° to 16.12° for (003) and (006) reflections, respectively), cf. Inset of Fig. 1 a. These changes are linked to a marked increase in the basal spacing of the most intense plane (003) from 7.17 to 10.60 Å on going from ZnAl-LDH-NO$_3$ to ZnAl-LDH-V$_{10}$O$_{28}$. Besides, the lattice parameter c of ZnAl-LDH-V$_{10}$O$_{28}$ is nearly one and half times that of ZnAl-LDH-NO$_3$, implying existence of remarkable packed stacks of typical brucite-like layers with a good ordering along the dimension c. As judged from Debye-Scherrer calculations, the average crystallite size of the brucite-type layers of ZnAl-LDH-V$_{10}$O$_{28}$ are radically reduced when compared with that of parent ZnAl-LDH-NO$_3$, recording about 8 nm length. All these facts are most probable indicative of successful intercalation of decavanadate anions into the interlayer spacing of Zn Al layered double hydroxide, guaranteeing pronounced substitution of NO$_3^-$ by V$_{10}$O$_{28}^{6-}$ ions. As is commonly known that the thickness of brucite-like sheets is equivalent to 4.8 Å [71], indexing of the (003) reflection and its basal spacing along the XRD pattern for ZnAl-LDH-V$_{10}$O$_{28}$ lead to a gallery height of 5.8 Å. Such value is a little-bit lower than those reported previously for similar decavanadate-intercalated LDH hybrid materials (~6.9 Å) by about a unit angstrom [17,24]. In an extraordinary trend, the relatively shorter gallery height observed here seems not to forestall the intercalation of V$_{10}$O$_{28}^{6-}$ ions inside the interlayer spacing of the host LDH material, whereas intercalation of decavanadate ions within the interlayer spacings of the basal (003) reflection of parent ZnAl-LDH-NO$_3$ is highly endorsed by the intimate interaction between the positively charged hydroxylated sheets (brucite-like layers) and the vanadium-oxygen bonds (V–O) of V$_{10}$O$_{28}^{6-}$ species either by electrostatic or hydrogen bonding [24,72,73]. Such interacting profile in ZnAl-LDH-V$_{10}$O$_{28}$ hybrid system presumably endows decavanadate ions with much more flexibility by which they can be persistently intercalated and oriented in the interlayer domain with their C_2 axis parallel to the brucite-like layers, being agreeable with previous studies [24,72–74]. This interaction behavior is further interpreted and approved by FT-IR and Raman spectroscopic analyses.

Alternately, in case of XRD pattern of ZnAl (H)-LDH-V$_{10}$O$_{28}$, the 2⊖ diffraction angles of the characteristic planes of brucite-like layers seem to be intermediate between those values referring to parent ZnAl-LDH-NO$_3$ and ZnAl-LDH-V$_{10}$O$_{28}$ hybrid sample, as the reflection at 2⊖ = 9.73° is indexed to basal (003) spacing of 8.7 Å, and that at 19.53° is ascribed to $d_{(006)}$ of 4.3 Å, see Fig. 1 a. These findings reveal that hydrothermal method is plausibly unable to expedite entire substitution of nitrate groups by decavanadate species within interlamellar spacing of LDH structure. This perception is also corroborated by extracting the gallery height from the basal spacing (003) of ZnAl (H)-LDH-V$_{10}$O$_{28}$, which shows a value (~3.9 Å) twofold smaller than those reported in literature for intercalating decavanadate ions inside brucite-like layers [17,24,74]. What's more, the non-basal XRD diffraction peaks in the parent ZnAl-LDH-NO$_3$ sample are kept unchanged by decavanadate intercalation into the interlayer spacing of LDH structure prepared by hydrothermal route (Fig. 1 a).

3.2. FT-IR and Raman studies

The chemical structures of the parent ZnAl-LDH-NO$_3$, and ZnAl-LDH-V$_{10}$O$_{28}$ as well as ZnAl (H)-LDH-V$_{10}$O$_{28}$ hybrid systems are investigated by FT-IR analysis (Fig. 1 b). For parent ZnAl-LDH-NO$_3$, strong absorption bands observed at ~3450 cm^{-1} and 1636 cm^{-1} can be attributed to the –OH stretching vibration in the brucite-like layers and the –OH bending vibration of interlayer water,

respectively [67,75]. A prominent peak at 1370 cm^{-1} corresponds to the stretching vibration of the nitrate anions within the interlayer of LDH structure [70]. In the lower wavenumber range (Fig. 1 b), the peak at 423 cm^{-1} and 556 cm^{-1} are ascribed to the O–Al–O and the Al–O–H stretching vibrations in the brucite-like layers [70,75], respectively. Besides, the weak absorption bands at 783 and 624 cm^{-1} are assigned to Al–OH and M − O (M–O–M or O–M–O; M = Zn, Al) bending deformation vibrations, respectively [68,70]. In case of ZnAl-LDH-V$_{10}$O$_{28}$ hybrid material, intercalation of decavanadate species into the interlamellar spacing does not impact the lattice vibrations of the host structure, keeping the absorption bands characteristic to the brucite-like layers at their original positions as observed in the FT-IR spectrum of parent ZnAl-LDH-NO$_3$, see Fig. 1 b. Moreover, the absorption band referring to nitrate ions in Fig. 1 b disappears accentuating fruitful intercalation of V$_{10}$O$_{28}^{6-}$ ions into interlayer spacing of LDH and their complete replacement for nitrate groups. As is also plotted in Fig. 1 b, the two characteristic vibration bands of V$_{10}$O$_{28}^{6-}$ species appear at 957 and 813 cm^{-1}, thus suggesting intercalation of decavanadate into interlayer spacings of LDH [74]. Of special interest, such intercalation profile seems to remove deformations from the brucite-like sheets, where the bands related to the deformation vibrations of LDH structure disappear (Fig. 1 b). This fact results in fabrication of well-defined brucite-like crystals, dealing with XRD data. Alternatively, the FT-IR spectrum of ZnAl (H)-LDH-V$_{10}$O$_{28}$ (Fig. 1 b) discloses existence of nitrate groups side by side with decavanadate species in the zinc aluminium LDH structure, alluding most probable to the incomplete substitution of NO$_3^-$ ions by the intercalating decavanadate anions.

Raman spectra of parent ZnAl-LDH-NO$_3$, ZnAl-LDH-V$_{10}$O$_{28}$ and ZnAl (H)-LDH-V$_{10}$O$_{28}$ samples are used to investigate the molecular composition, and to better verify the existence of decavanadate species, as declared in Fig. 1 c. The spectrum of ZnAl-LDH-NO$_3$ presents bands at 479 and 563 cm^{-1} belonged to the lattice stretching vibrations of the brucite octahedral layers, i.e., Al –O–Mg, Zn–OH and Al–OH [26,75]. Also, the band at 1060 and 713 cm^{-1} are credited to the nitrate stretching vibrations [75,76]. Comparing to the Raman analysis of parent ZnAl-LDH-NO$_3$ sample, the Raman spectrum of ZnAl-LDH-V$_{10}$O$_{28}$ nanohybrid material (Fig. 1 c) displays new bands predictable at 996, 595, and 334 cm^{-1}, which concurred with characteristic bands assigned in literature to decavanadate species [26, 77,78]. The sharp and the most intense band observed at 996 cm^{-1} corresponds to the V–O stretching mode of terminal V=O groups [26,77]. The Raman spectra for this nanohybrid sample also indicates the absence of any residual NO$_3^-$ anions reflecting their fulfil substitution by V$_{10}$O$_{28}^{6-}$ ions with the help of anion exchange process, thus facilitates decavanadate intercalation. As a consequence, the local environment in the interlayer spaces of the brucite-like layers is plausibly changed, where these layers are imposed to tightly interact with decavanadate species. Hence, marked shifting of the brucite lattice vibrations of ZnAl-LDH-V$_{10}$O$_{28}$ to lower frequencies is remarkably observed, compared with those of ZnAl-LDH-NO$_3$ (Fig. 1 c). This aspect is coincident with the results documented by Dobrea et al. [26], which disseminated that intercalation of polyoxometalates into layered double hydroxides may possibly cause the presence of strong cation-anion interactions. On the contrary, Raman spectrum of ZnAl (H)-LDH-V$_{10}$O$_{28}$ exhibits vibration bands characteristic to both nitrate and decavanadate ions linked with keeping the stretching vibrational bands of the brucite octahedral layers very close to those distinguished from the Raman pattern of ZnAl-LDH-V$_{10}$O$_{28}$ nanohybrid sample, cf. Fig. 1 c. These facts possibly reflect the incapability of hydrothermal route to efficiently proceed ion-exchange process resulting in (i) deficient replacement of NO$_3^-$ by decavanadate anions, (ii) poor interaction of V$_{10}$O$_{28}^{6-}$ with ZnAl-LDH nanosheets, and (iii) limited intercalation of decavanadate ions into LDH interlayer galleries.

3.3. XPS analysis

The surface chemical composition and the electronic structure of the parent ZnAl-LDH-NO$_3$, nanohybrid ZnAl-LDH-V$_{10}$O$_{28}$, and ZnAl (H)-LDH-V$_{10}$O$_{28}$ sample are identified using XPS analysis (Fig. S1 in the supplementary materials, and Fig. 2). For parent ZnAl-LDH-NO$_3$, the XPS survey shows the presence of Zn, Al, O, and N elements (Fig. S1 a, supplementary materials). Meanwhile, the XPS survey of ZnAl-LDH-V$_{10}$O$_{28}$ displays spectral features of the elements Zn, Al, and O with additional feature of V, reflecting successful exchanging of nitrate groups by decavanadate species within the interlamellar spacing of the LDH structure, Fig. S1 a (supplementary materials). As visualized in Fig. 2 a, the parent ZnAl-LDH-NO$_3$ sample exhibits two distinct peaks at binding energies of 1046.3 eV and 1022.7 eV that arise from the spin-orbit splitting into Zn 2p$_{1/2}$ and Zn 2p$_{3/2}$ components, respectively [21,79]. The binding energy characteristic to Al element in ZnAl-LDH-NO$_3$ sample appears as a broad peak (Fig. 2 b), which are deconvoluted into two spin-orbital signals of Al 2p$_{1/2}$ and Al 2p$_{3/2}$ at binding energies of 75.9 eV and 74.1 eV, respectively [21,80]. As plotted in Fig. 2 (a, b), the characteristic signatures of the Zn^{2+} and Al^{3+} in the layered structure of ZnAl-LDH-V$_{10}$O$_{28}$ nanohybrid material are noticeably shifted to lower binding energies compared to those assigned to parent ZnAl-LDH-NO$_3$, whereas the spin doublets being located at 1043.2 eV (Zn 2p$_{1/2}$), 1019.9 eV (Zn 2p$_{3/2}$), 75.4 eV (Al 2p$_{1/2}$), and 73.4 eV (Al 2p$_{3/2}$). These chemical shifts may strongly confirm the intercalative hybridization of LDH with V$_{10}$O$_{28}^{6-}$ species. The developed anionic character of the intercalated decavanadate species not only favours screening the valence electrons of Zn and Al elements in the ZnAl-LDH-V$_{10}$O$_{28}$ nanohybrid sample, but also facilitates donation of electrons to the Zn^{2+} and Al^{3+} ions in the LDH structure, thus creating different modes of interaction. This assertion runs in harmony with XRD, FT-IR, and Raman results. As shown in Fig. 2 c, the high-resolution V2p XPS spectrum of ZnAl-LDH-V$_{10}$O$_{28}$ nanohybrid sample registers two signals at 525.5 eV (V 2p$_{1/2}$) and 518.4 eV (V 2p$_{3/2}$) [79,81], presumably indicates presence of vanadium species with a pentavalency in the interlayer space of zinc aluminium LDH, as being verified from FT-IR and Raman data.

Further affirmation to the intimate interaction between V$_{10}$O$_{28}^{6-}$ species and brucite-type layers can be deduced from studying the O1s XPS spectra of the parent ZnAl-LDH-NO$_3$ and ZnAl-LDH-V$_{10}$O$_{28}$ nanohybrid sample, Fig. 2 d. The O1s satellite peak of ZnAl-LDH-NO$_3$ sample is convoluted into two components. The peak X located at a binding energy of ~531.8 eV is attributed to the OH group of brucite layer [11,79], while the peak Y situated at ~532.9 eV refers to the binding energy of O in the hydroxyl (or crystal water) adsorbed on the interlayer surfaces [81]. Conceivably, the very same trend, in the light of lower shifting of Zn2p and Al2p XPS spectra of ZnAl-LDH-V$_{10}$O$_{28}$ in comparison with those of parent ZnAl-LDH-NO$_3$, is observed from the XPS feature of O in ZnAl-LDH-V$_{10}$O$_{28}$ nanohybrid material; so that the negative shift in the O1s X (530.5 eV) and Y (532.2 eV) binding energies (Fig. 2 d) attributes to the
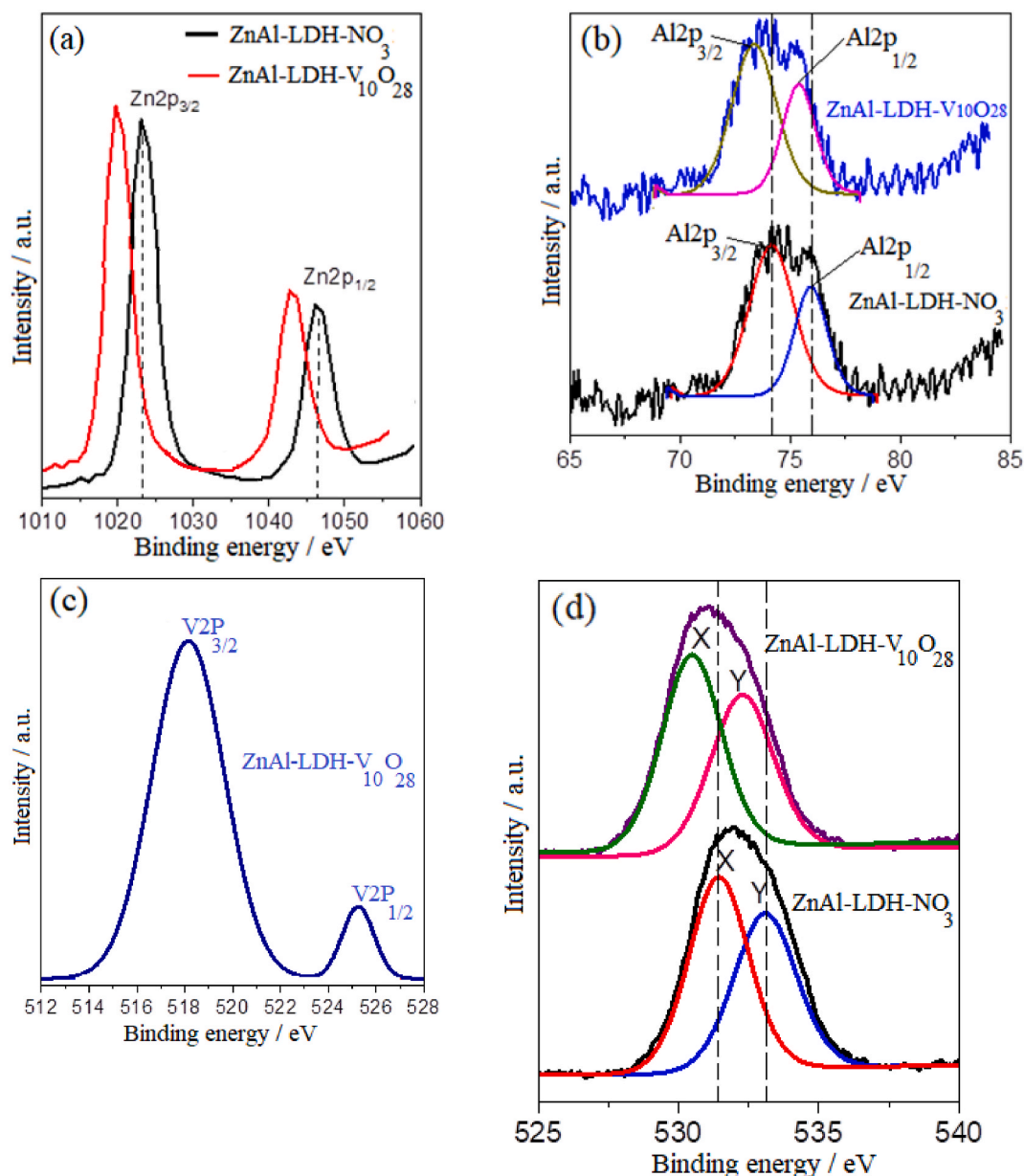
Fig. 2. High-resolution XPS spectra of: Zn2p (a), Al2p (b), V2p (c), and O1s (d) of the samples under study.

enhanced electron density on the host ZnAl-LDH nanosheets in virtue of their effective electronic coupling with the guest decavanadate anions. As regards, intercalation of decavanadate anions in the interlayer galleries of LDH and their firm interaction to the hydroxyl groups of brucite-like layers are vividly established by activating the hydrothermal treatment of ZnAl-LDH-$V_{10}O_{28}$ hybrid material with microwave irradiation.

For better understanding the deep impact of microwave irradiation in tailoring the decavanadate intercalated ZnAl layered double hydroxide nanohybrid sample during the hydrothermal treatment, the XPS survey as well as XPS spectra features of ZnAl (H)-LDH-$V_{10}O_{28}$ hybrid sample are implemented and illustrated in in the supplementary materials. It is worth noting that ZnAl (H)-LDH-$V_{10}O_{28}$ sample contains Zn, Al, N, V, and O elements, where the binding energies of Zn2p, Al2p, and O1s core levels in this hybrid sample most probable appear at similar positions to those of parent ZnAl-LDH-NO_3. These results strongly suggest that intercalative hybridization of LDH with $V_{10}O_{28}^{6-}$ cannot be efficiently take place during the hydrothermal treatment, which not only limits the substitution of NO_3^- groups by decavanadate ions, but also restricts the interaction between intercalating anions and host cationic LDH sheets, coping with XRD, FT-IR, and Raman analyses. Henceforth, it is noteworthy to study the morphological, textural, surface charge, and conductivity characteristics of ZnAl-LDH-$V_{10}O_{28}$ nanohybrid sample in comparison with those of parent ZnAl-LDH-NO_3 sample.

3.4. SEM/EDX and HR-TEM studies

The morphology and structure characteristics of the parent ZnAl-LDH-NO$_3$ sample as well as ZnAl-LDH-V$_{10}$O$_{28}$ nanohybrid material are investigated using SEM/EDX analysis, as demonstrated in Fig. 3 (a, b) and supplementary document in Fig. S2. It can be easily envisaged that the parent ZnAl-LDH-NO$_3$ possesses heterogenous aggregates of platelet morphology with distinctly cracked edges, Fig. 3a, i. These aggregates exhibit an average diameter ranging between 13 and 50 μm (Fig. 3a, i). This acquired representative feature is distinctive for the zinc aluminium LDH synthesized by co-precipitation route [82,83]. As shown from the EDX analysis of parent ZnAl-LDH-NO$_3$ (Fig. 3a, ii), zinc, aluminium, nitrogen and oxygen elements are present in the LDH structures, and an atomic ratio of 1.8:1 is estimated for Zn:Al which coincides with the nominal amounts of Zn and Al used in the preparation of this sample.

As shown in Fig. 3b (i), ZnAl-LDH-V$_{10}$O$_{28}$ hybrid sample, which is obtained by facilitating anion exchange of NO$_3^-$ with V$_{10}$O$_{28}^{6-}$ using microwave-assisted hydrothermal method, displays separated well-dimensioned blocks of homogeneous planar surfaces, as represented by elements 1–5, linked with presence of sharp edges (as labelled by yellow arrows). These blocks exhibit a broad size range, with diameters ranging from 10 μm to 57 μm, meanwhile most of them have an average lateral size of 6 μm (Fig. 3b, i). As can be
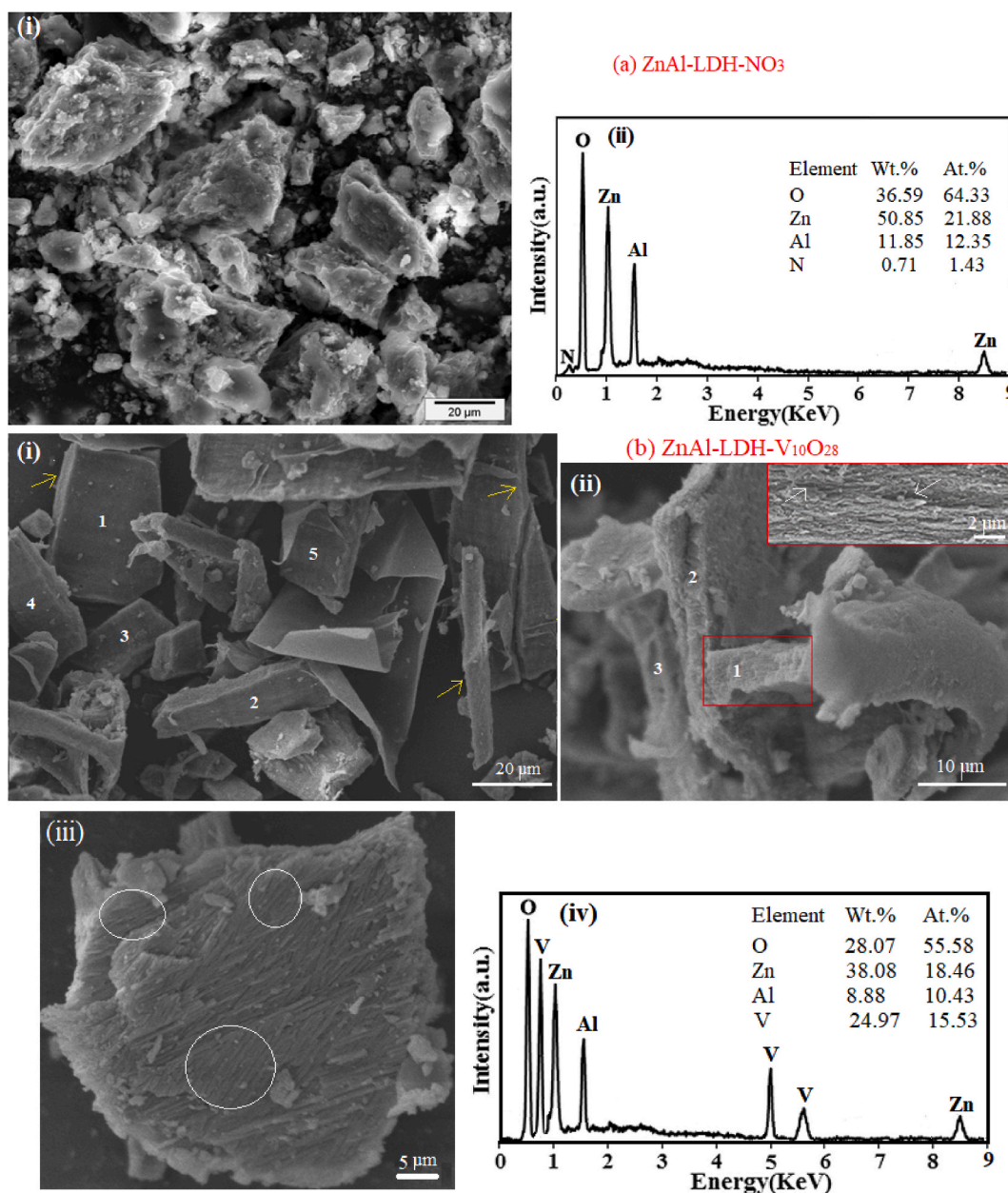
Fig. 3. SEM micrographs for samples under investigation, and their corresponding EDX patterns in images a (ii) and b (iv).

(a) ZnAl-LDH-NO₃
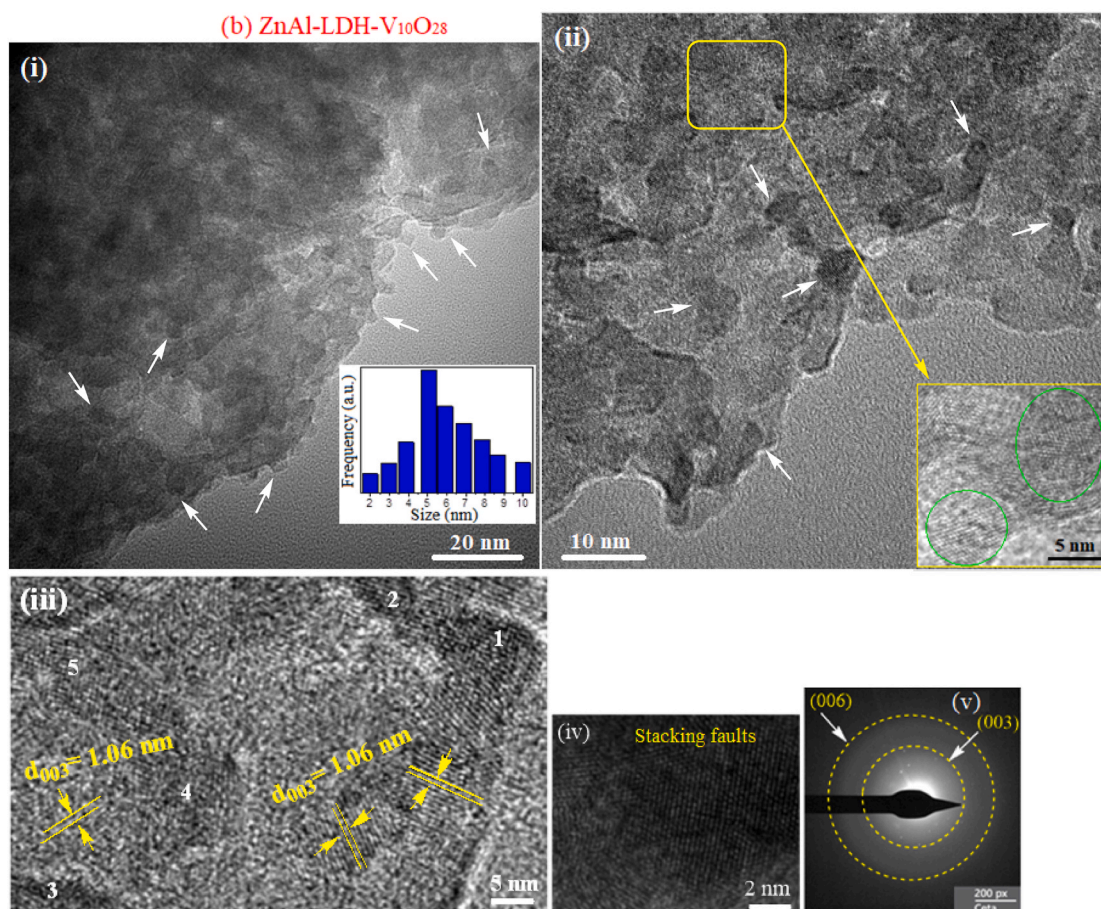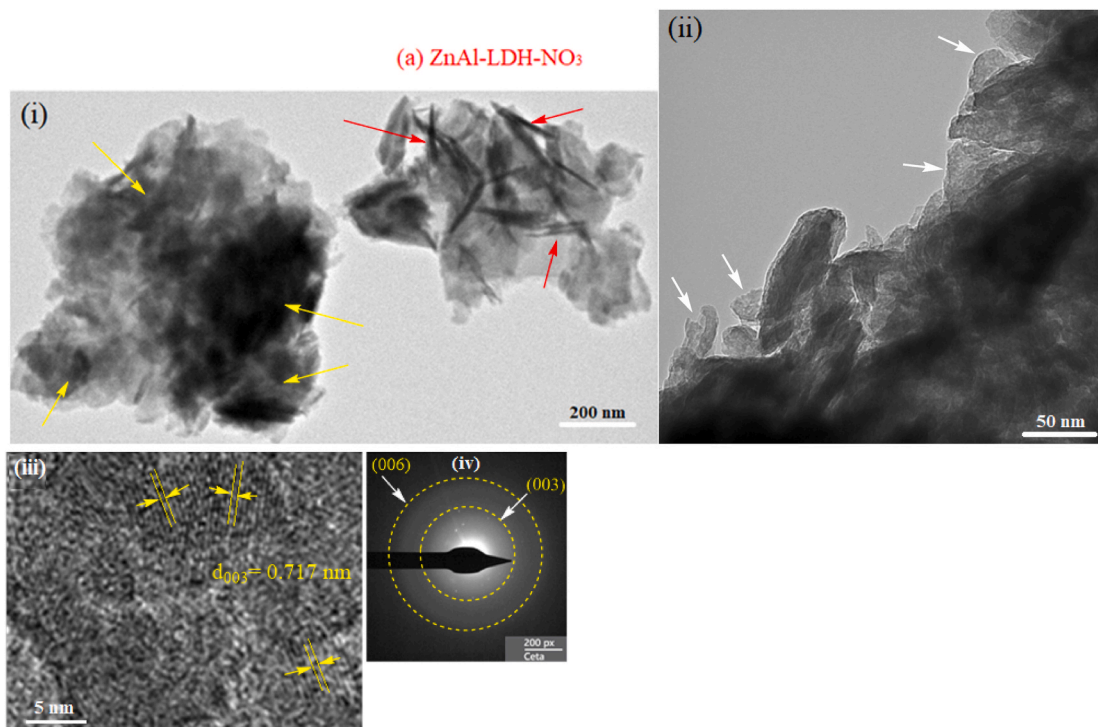
(b) ZnAl-LDH-V₁₀O₂₈

(caption on next page)

Fig. 4. TEM micrographs of parent ZnAl-LDH-NO$_3$ and ZnAl-LDH-V$_{10}$O$_{28}$ nanohybrid samples, and their corresponding electron diffraction patterns. The inset image in figure b (i) shows the particle size distribution histogram.

seen in Fig. 3b (ii), each block plausibly comprises of a set of stacking brucite-like layers of hierarchical architecture, as represented by elements 1–3. Given more clearness to the hierarchical morphology of ZnAl-LDH in the hybrid sample, the inset image of Fig. 3b (ii), as the contents in the red-lined rectangular area are magnified, strongly deduces that occupation of V$_{10}$O$_{28}^{6-}$ species to the interlamellar spacing of ZnAl-LDH-V$_{10}$O$_{28}$ sample effectively improves the aligned arrangement of LDH – in other words, provokes stacking of brucite-like layers in a parallel orientational conformation. Speaking to the XRD, FT-IR, Raman, and XPS results, the stacked hierarchical morphology of the brucite-like layers in ZnAl-LDH-V$_{10}$O$_{28}$ sample is enthusiastically supported by the acquired respective strong interaction between the positively charged LDH, which is enriched with -OH groups, and the decavanadate anions; a provision which is previously devoted by Varadwaj and Nyamori [20] and Guo et al. [84]. As shown from the top view of a unit LDH block in ZnAl-LDH-V$_{10}$O$_{28}$ nanohybrid sample (Fig. 3b, iii), intercalation of LDH structure by V$_{10}$O$_{28}^{6-}$ species induces existence of the densely hierarchical stack of brucite-like layers linked with an extended regular parallel orientation, as signified by the white circles. In this respect, the parallel assembly of decavanadate-intercalated brucite-like layers perhaps restrains the aggregation of LDH, affording an open hierarchical structure (see white arrows in the inset of Fig. 3b, ii) with a developed intragallery porosity and surface area expansion, as being latter discussed by surface analysis. The hierarchical architecture of ZnAl-LDH-V$_{10}$O$_{28}$ nanohybrid sample most likely matches the hierarchical structure features of both graphene/Ni–Al LDH nanocomposite and TiO$_2$/cellulose nanofibers, where the base materials are assembled orderly and stacked densely [20,84]. The discrepancy in the morphological properties of the two understudied samples may possibly attribute to the notable difference in the size, charge density, and chemical nature of nitrate ions and decavanadate ones. From seeing in Fig. 3b (iv), the EDX spectrum of ZnAl-LDH-V$_{10}$O$_{28}$ contains O, Zn, Al, and V elements linked with Zn/Al atomic ratio relevant to that recorded by parent ZnAl-LDH-NO$_3$, thus reveals the proficiency of LDH structure to significantly host decavanadate species in its interlamellar spacing. The mass percentages of the O, Zn, Al, and V atoms in the prepared ZnAl-LDH-V$_{10}$O$_{28}$ nanohybrid sample are confirmed by the EDX results, cf. Fig. 3b (iv). Moreover, the peak corresponding to nitrogen element is vanished in the EDX pattern of ZnAl-LDH-V$_{10}$O$_{28}$ (Fig. 3b, iv) suggesting successful exchange of nitrate ions with decavanadate ones, thus endorsing Raman and XPS results. A closer look at the SEM/EDX microstructure image of the ZnAl-LDH-V$_{10}$O$_{28}$ sample and its corresponding elemental mapping are delineated in the supplementary file, . The distribution maps of Zn, Al, O, and V elements are represented in green, red, blue, and yellow colours, respectively (supplementary file, Fig. S2 (b-e)). The absence of each element is shown in black. From these SEM/EDX mapped regions, it is clearly obvious that the composition map of Zn and O elements are homogeneously distributed in the specimen (supporting file, Fig. S2 (b, d). The mapping analysis of Al element seemingly shows little-bit areas of Al accumulation with a non-homogeneous distribution, although average homogeneity is maintained, cf. Fig. S2 (c), supplementary material. As is evidenced from Fig. S2 (e), supporting material, the V element is uniformly distributed throughout the zinc aluminium LDH matrix.

For better understanding the microstructure and crystallographic texture of parent ZnAl-LDH-NO$_3$ and ZnAl-LDH-V$_{10}$O$_{28}$ nanohybrid samples, TEM analysis was performed and represented in Fig. 4 (a, b). The top view TEM image of the parent ZnAl-LDH-NO$_3$ sample clearly displays random aggregates of brucite crystallites with platelet-like morphology (see yellow arrows in Fig. 4a, i) accompanied by presence of disordered filamentous formations (as shown by the red arrows in Fig. 4a, i). A careful inspection deduces that formation of fibrous structure is most probably caused by the presence of defects in the brucite-like structure of ZnAl-LDH-NO$_3$, as being evidenced from XRD and FT-IR data. The layered structure of parent ZnAl-LDH-NO$_3$ is further distinguished in Fig. 4a, ii, displaying presence of barely coherent brucite-like sheets with an average length of 34 nm (cf. White arrows). As illustrated in Fig. 4a, iii, the lattice fringes with a distance of ~0.717 nm can be indexed to the basal spacing of (003) plane in the brucite-like structure of ZnAl-LDH-NO$_3$ sample. Selected area electron diffraction pattern (SAED) pattern (Fig. 4a, vi) reflects the periodic diffraction concentric rings indexed to (003) and (006) planes revealing the nanocrystalline nature of the parent ZnAl-LDH-NO$_3$ sample. These findings are in line with the previous reports [67,85], being coincide with those distinguished from XRD data.

As extracted from the HR-TEM images in Fig. 4b (i, ii), intercalation of decavanadate ions into the interlayer spaces of Zn Al brucite-like layers seems to fractionalize the LDH sheets and reduce their dimensions, thus yielding nanosized layers of lengths around 6 nm, as represented by the white arrows in Fig. 4 b (i and ii). The nanosized layered structure of ZnAl-LDH-V$_{10}$O$_{28}$ sample is further verified by investigating its corresponding particle size distribution plot, which assesses an average particle size of ~6 nm, inset of Fig. 4 b (i). This finding copes with XRD data. It is worthwhile to also note that the brucite-like layers in ZnAl-LDH-V$_{10}$O$_{28}$ nanohybrid appear to be much more separated with lesser aggregation forms rather than those observed in parent ZnAl-LDH-NO$_3$ sample, cf. Fig. 4 b (i and ii). By magnifying the contents in the yellow-lined area in Fig. 4b (ii), the less dense aggregating brucite-like sheets are most probably stacked, whereas separated ensembles of aligned and equally-spaced parallel dark lines seem to appear, as represented by the green circles in the inset of Fig. 4b (ii). Such stacking orientation of the brucite-like layers is further clarified by the presence of series of interconnected and/or stacking faults of equally-spaced lattice fringes, as shown by elements 1–5 in Fig. 4b (iii) and Fig. 4b (iv). This assertion is obviously proved by FT-IR, Raman and XPS results, which confirm the accessibility of microwave-hydrothermal route to conduct firm interaction between brucite-like layers and the intercalating decavanadate anions. At this juncture, the acquired respective fault zones may possibly lead to a layered double hydroxide structure enriched with hierarchy view, as being evidenced from the SEM investigation of ZnAl-LDH-V$_{10}$O$_{28}$ sample. On this basis, the pore structure of ZnAl-LDH-V$_{10}$O$_{28}$ nanohybrid sample can be assertively developed highlighting expansion of surface area and formation of mesopores, as discussed below in Sec. *3.5*. As shown in Fig. 4b (iii), the measured crystal plane distance referred to the (003) lattice plane, which belongs to the LDH structure of ZnAl-LDH-V$_{10}$O$_{28}$, is significantly enlarged registering d-spacing of *ca.* 1.06 nm, thus indicates remarkable intercalation of V$_{10}$O$_{28}^{6}$ ions within the

interlayer spacing of the LDH structure. This result concurs with XRD, FT-IR, Raman, and XPS results. The SAED pattern of ZnAl-LDH-$V_{10}O_{28}$ nanohybrid is analogue to that of parent ZnAl-LDH-NO_3, Fig. 4b (v).

3.5. Surface analysis

The textural characteristics of parent ZnAl-LDH-NO_3 and ZnAl-LDH-$V_{10}O_{28}$ nanohybrid samples are determined through N_2 adsorption-desorption isotherm measurements as depicted in Fig. 5 (a, b). It is evident that all the provided adsorption isotherms can be categorized as Brunauer-Deming-Deming-Teller (BDDT) type-IV isotherm shapes and H3-type hysteresis loops based on IUPAC classification, reflecting possible existence of aggregates of plate-like particles with slit shape mesopores [11,85]. For parent ZnAl-LDH-NO_3 sample, the N_2 adsorption increases fairly slow up to P/P_o ~0.75 and finally rapid near the saturation pressure linked with a hysteresis loop in the range 0.75–0.99 P/P_o, Fig. 5a. Meanwhile, in case of ZnAl-LDH-$V_{10}O_{28}$ nanohybrid, the adsorption branch is steeply increased over the whole P/P_o range, i.e., recording values higher than that of parent ZnAl-LDH-NO_3, accompanied by presence of a distinct hysteresis loop that covers an extended P/P_o region ranged from 0.45 to 0.99 (Fig. 5a). The N_2 adsorption-desorption isotherm of ZnAl-LDH-$V_{10}O_{28}$ nanohybrid alludes to the presence of well-ordered and slit-shaped mesopores, which probably contain narrow and wide fragments as well as interconnecting channels. The surface parameters derived from the N_2 adsorption-desorption isotherms of the understudied samples are investigated and scheduled in Table 1. Comparing to parent ZnAl-LDH-NO_3, the surface area (S), total pore volume (V_p), and average pore radius (r_p) of ZnAl-LDH-$V_{10}O_{28}$ nanohybrid sample are significantly increased, viz., from 26 to 44 $m^2\,g^{-1}$, from 0.1245 to 0.2218 $ml\,g^{-1}$, and from 80 to 120 Å, respectively. With regard to the expanded gallery height of ZnAl-LDH-$V_{10}O_{28}$ compared with that of ZnAl-LDH-NO_3, as deduced from the respective XRD patterns, it is noted that the marked expansion in the S, V_p, and r_p values of ZnAl-LDH-$V_{10}O_{28}$ sample might possibly be attributed to the hierarchy stacking structure of the brucite-like layers, fact that vividly offers advanced mesoporous spaces. Furthermore, the pore size distribution curves of the parent ZnAl-LDH-NO_3 and ZnAl-LDH-$V_{10}O_{28}$ are also studied (Fig. 5b). It deserves mentioning that all the understudied samples exhibit a mesoporous structure, which results majorly from the interparticle spaces with reasonable contribution to the LDH interlayer spacing. The parent ZnAl-LDH-NO_3 sample displays a broad pore size distribution covering a diameter range of ~10–38 nm accompanied by presence of small fractions of mesopores with diameter ranged from 2 to 4.3 nm, Fig. 5b and its inset
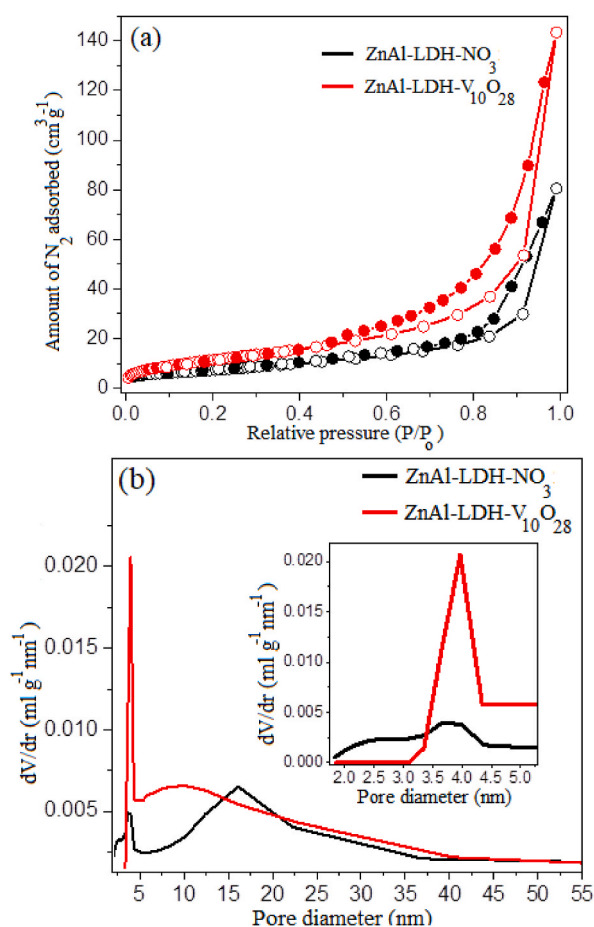
Fig. 5. (A) N_2 adsorption-desorption isotherms and (b) pore size distribution curves of the samples under investigation.

Table 1

Surface textural parameters derived from N_2- adsorption/desorption isotherms of samples under investigation.

Samples	S (m^2 g^{-1})	V_P (ml g^{-1})	r_P (Å)	$\bar{r}_h$ (Å)
ZnAl-LDH-NO$_3$	26	0.1245	80	20 - 43, 100 - 376
ZnAl-LDH-V$_{10}$O$_{28}$	44	0.2218	120	40, 60 - 400

image, and Table 1. Otherwise, developed and well-defined pore size distribution curve is observed for ZnAl-LDH-V$_{10}$O$_{28}$ hybrid sample, as larger fractions of mesopores with broad and intense distribution appear at pore diameter in the range 6–40 nm (Table 1 and Fig. 5b). Besides, a shake-up peak referred to populations of mesopore fractions with an average diameter of *ca.* 4 nm appears, see the inset of Fig. 5b. All these results outline that the advanced mesoporous structure of ZnAl-LDH-V$_{10}$O$_{28}$ sample, compared to parent ZnAl-LDH-NO$_3$, can be emanated from the accessibility of LDH gallery height upon intercalative hybridization with decavanadate ions, where the V$_{10}$O$_{28}^{-6}$ species encourage formation of new interparticle and intragallery porosity, and accommodates existence of unusual interconnections of multiple LDH plates. By this way, the notable mesoporosity of the ZnAl-LDH-V$_{10}$O$_{28}$ nanohybrid may be strongly signified as evidence for the presence of hierarchically stacked brucite-like layers, as demonstrated from SEM and HR-TEM investigations.

3.6. Surface charge analysis and conductivity study

The obtained zeta-potential and particle size distribution curves, and conductivity measurements of parent ZnAl-LDH-NO$_3$ and ZnAl-LDH-V$_{10}$O$_{28}$ nanohybrid are illustrated in Fig. 6(a–c). By intercalative stabilization of decavanadate ions into the interlamellar spaces of zinc aluminium LDH structure and efficacious substitution of nitrate groups by V$_{10}$O$_{28}^{-6}$ species, the sharp unimodal peak of the parent ZnAl-LDH-NO$_3$ sample at ζ_{av} ~16.67 mV is notably shifted to lower zeta-potential values in case of ZnAl-LDH-V$_{10}$O$_{28}$ nanohybrid sample recording twofold decreasing ζ_{av} value (~8.84 mV), Fig. 6a (i, ii), i.e., the charge homogeneity in the layered structure of LDH is attained in both samples and the sharp profile of their zeta-potential distribution curves are radically unchanged. Turning to the electronic nature of the interlayer anions within the gallery height of the LDH structure, occupation of the interlayer region to monovalent anions like nitrate groups is insufficient to entirely balance the positively charged LDH sheets, conducting
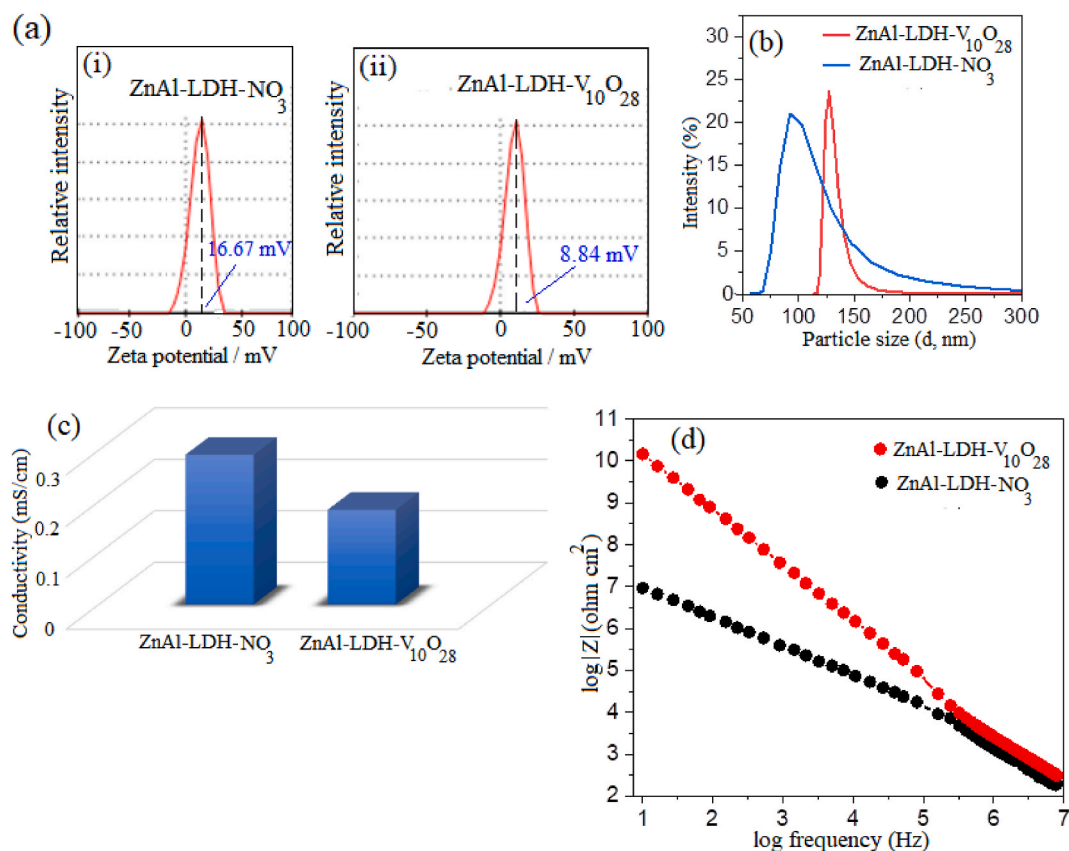
Fig. 6. (A) Zeta-potential distribution curves, (b) hydrodynamic particle size distribution profiles, (c) conductivity, and (d) Bode plots of parent ZnAl-LDH-NO$_3$ and nanohybrid ZnAl-LDH-V$_{10}$O$_{28}$ samples.

(A)

(B)
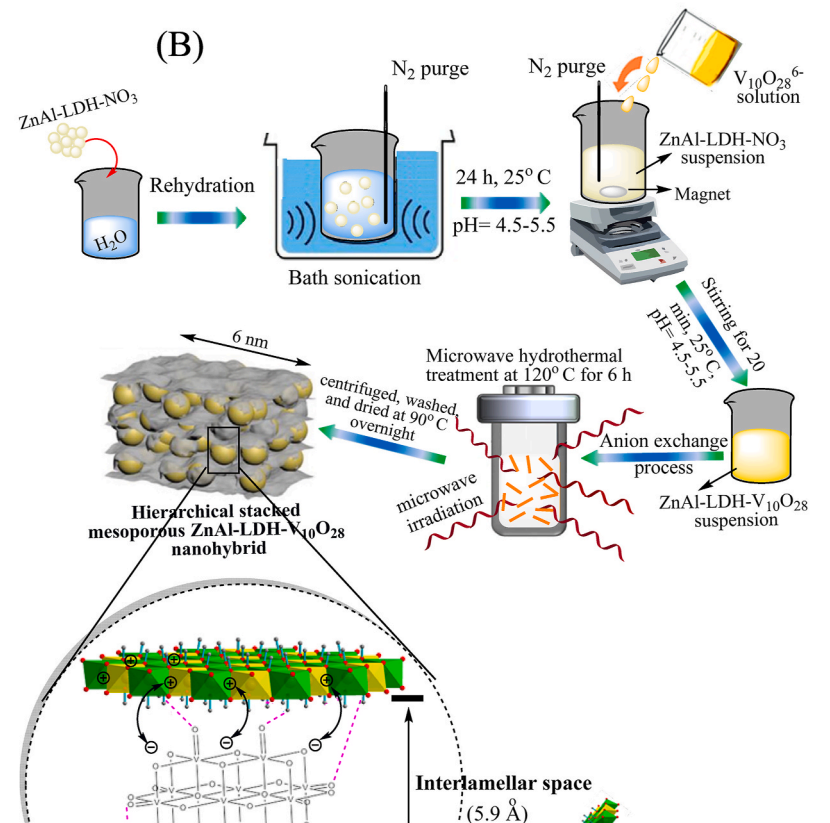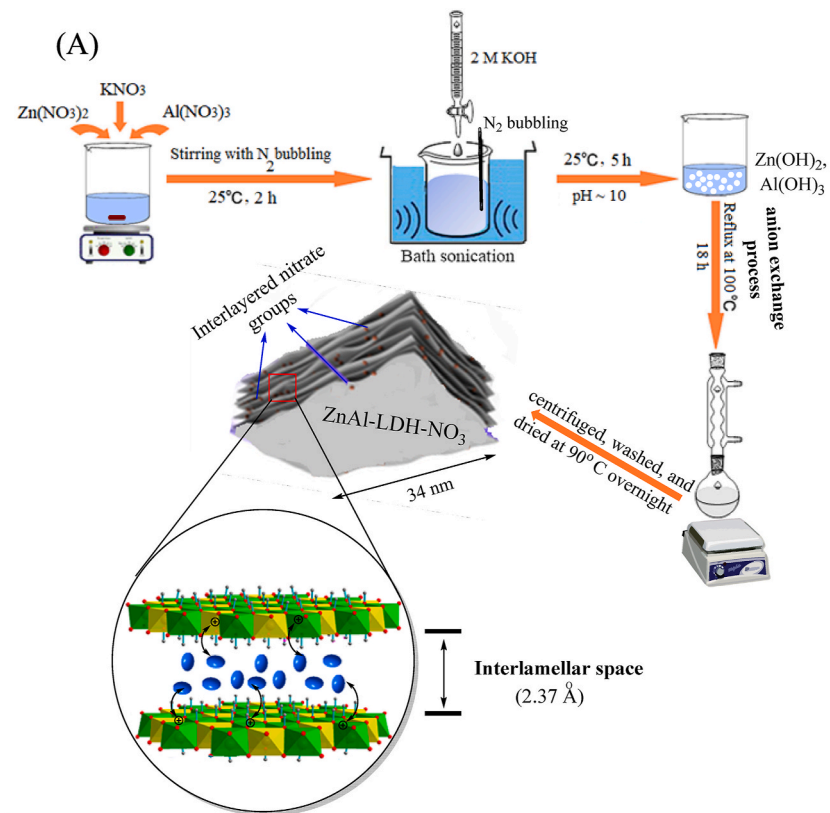
Fig. 7. (A) Preparation procedure of parent ZnAl-LDH-NO$_3$ sample via co-precipitation method and (B) synthetic route of ZnAl-LDH-V$_{10}$O$_{28}$ nanohybrid using microwave-assisted hydrothermal method, describing the proposed interaction profiles within their interlayer galleries.

surfaces with pronounced zeta-potential values (Fig. 6a, i). Meanwhile, intercalation of decavanadate species (as a typical hexavalent anion) into the interlayer spaces of the LDH structure via ion-exchange process can efficiently compensate the positive charges on the LDH lamellar, yielding surfaces of poor zeta-potential values (being close to neutrality) (Fig. 6a, ii). This perception is further verified by studying the hydrodynamic particle size distribution curves of the understudied sample. Broad and intense peak belonging to the particle size distribution profile of parent ZnAl-LDH-NO$_3$ sample appear, displaying diameters ranging from 60 nm to 300 nm with an average size of *ca.* 97 nm (Fig. 6b). On contrary, the hydrodynamic size distribution curve of the nanohybrid ZnAl-LDH-V$_{10}$O$_{28}$ sample shows a sharp and strong peak at a particle size of ~128 nm, i.e., being nearly twofold greater than that recorded by ZnAl-LDH-NO$_3$ sample, Fig. 6b. The estimated particle sizes of the understudied samples from SEM and DLS analyses are much higher than those extracted from XRD and HR-TEM studies, reflecting the confined ability of SEM and DLS measurements to distinguish the aggregated stacks of brucite-like crystals, in particular, the LDH stacks that are formed by intercalating decavanadate ions in between the interlayers of LDH structure.

Comparing to ZnAl-LDH-NO$_3$ sample, the marked reduction in the conductivity of ZnAl-LDH-V$_{10}$O$_{28}$ is often a consequence of
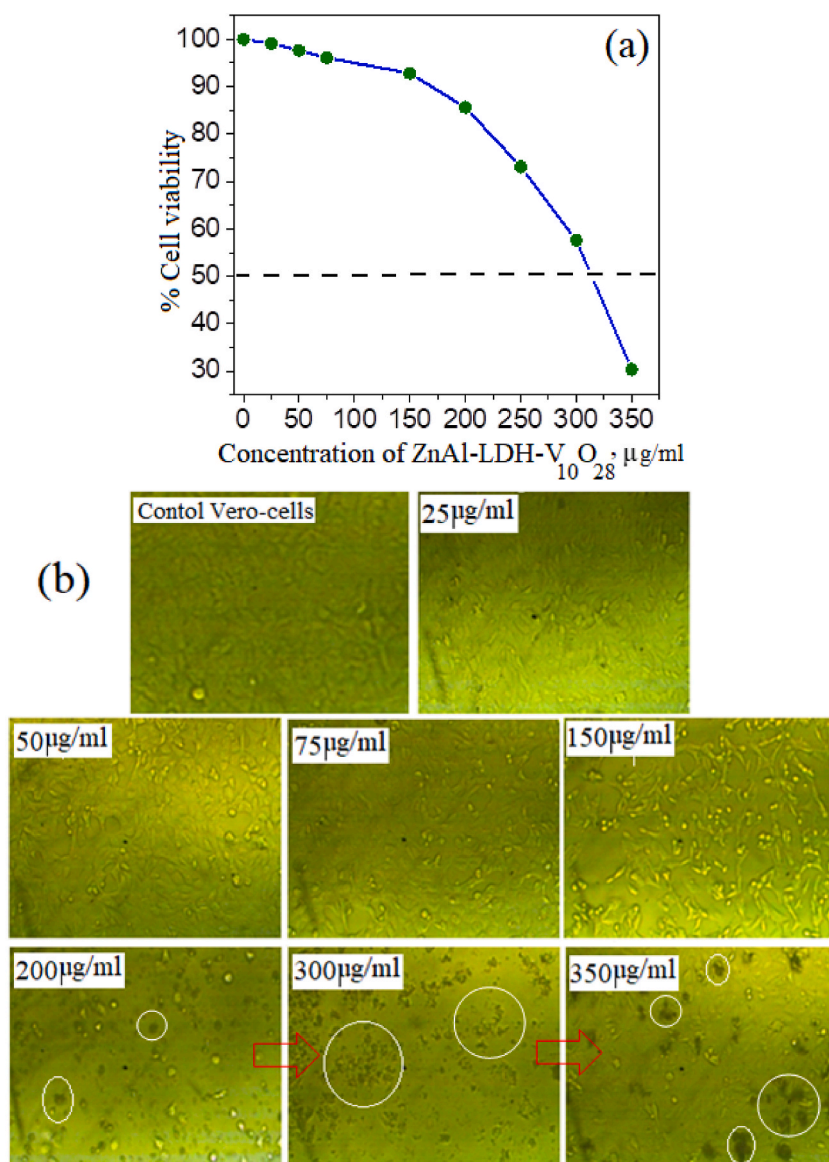
Fig. 8. (A) % cell viability of the ZnAl-LDH-V$_{10}$O$_{28}$ nanohybrid after 24 h incubation in Vero cell line at different concentrations, and (b) their corresponding microscopic images in comparison to the photomicrograph of control Vero cells.

decrement in the zeta-potential values and increment in the hydrodynamic particle sizes (Fig. 6(a–c)), suggesting the densely hierarchical stacking of the brucite-like layers in ZnAl-LDH-$V_{10}O_{28}$ hybrid sample. Such layered stacking justification is closely congruent with SEM and HR-TEM data.

To better understand the electrical nature of the as-prepared LDH samples, the real part impedance (Z) as a function of frequency for ZnAl-LDH-NO_3 and ZnAl-LDH-$V_{10}O_{28}$ samples is elucidated and depicted in Fig. 6d. The nanohybrid ZnAl-LDH-$V_{10}O_{28}$ sample exhibits much higher impedance than that of parent ZnAl-LDH-NO_3 (Fig. 6d), conceivably hypothesizes that exchanging of nitrate groups by decavanadate ions in the LDH interlayer galleries stimulates the charge-transfer resistance and diminishes the charge separation. These findings most probably arouse from (i) the high compensation effect of $V_{10}O_{28}^{6-}$ species on the cationic lamellar zinc aluminium LDH structure, as being evidenced from the zeta-potential study, and (ii) the densely hierarchical stack and intimate interaction of brucite-like layers with the intercalating decavanadate anions, as verified by FT-IR, Raman, XPS, SEM, and HR-TEM studies. These results are in margins with literature data [10,29].
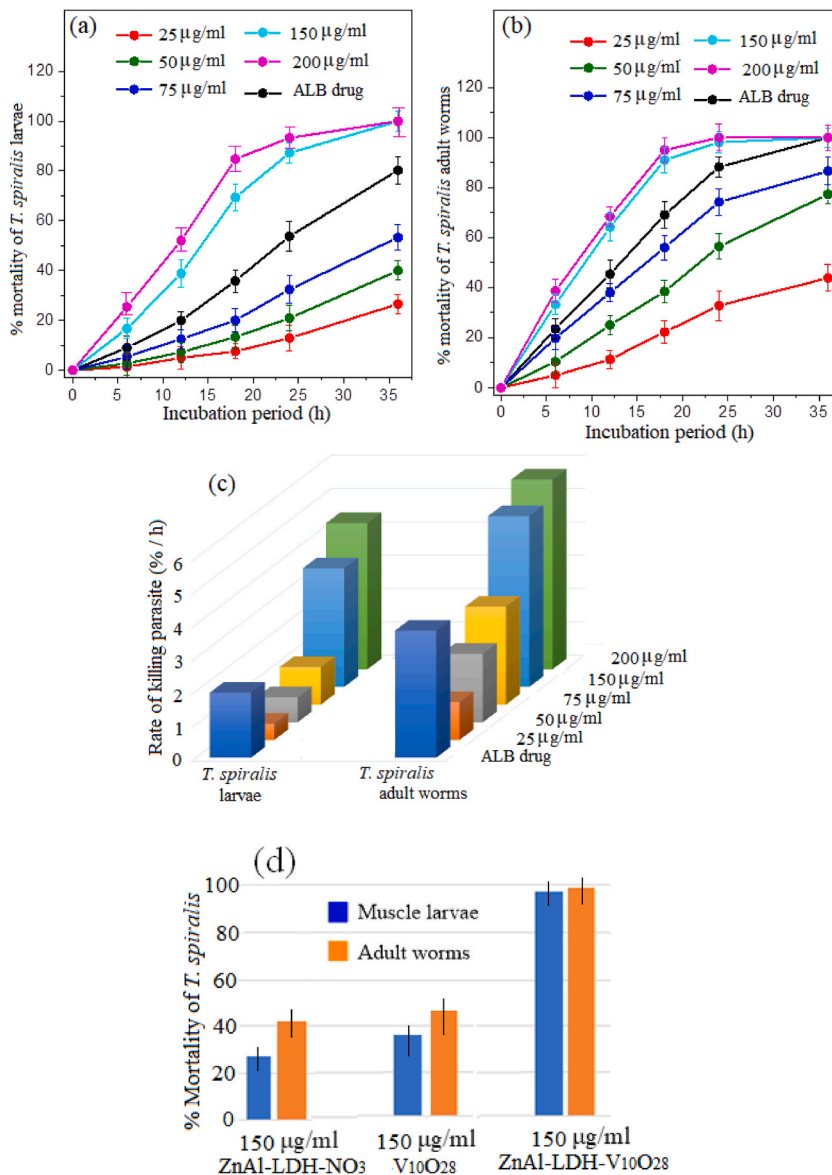
Fig. 9. Time- and dose-response curves of *T. spiralis* muscle larvae (a) and adult worms (b) against % parasite mortality when exposed to ZnAl-LDH-$V_{10}O_{28}$ nanohybrid for 36 h. Rate of killing of muscle larvae and adult worms of *T. spiralis* (c) using different dosages of ZnAl-LDH-$V_{10}O_{28}$ nanohybrid. % Mortality of *T. spiralis* muscle larvae and adult worms (d) using 150 μg/ml concentration of ZnAl-LDH-NO_3 sample and $V_{10}O_{28}$ solution in comparison to 150 μg/ml ZnAl-LDH-$V_{10}O_{28}$ hybrid sample after 36 h of incubation. For comparative reference, the % mortality as well as the rate of killing of different *T. spiralis* developmental stages using ALB drug at concentration of 30 μg/ml are indicated. Note that the bars show the range of dead worms percentages in the examined experiments.

Based on the forgoing physicochemical characteristics of the as-prepared LDH samples, portrayal view for the synthetic routes of ZnAl-LDH-NO$_3$ and ZnAl-LDH-V$_{10}$O$_{28}$ samples are represented in Fig. 7 (A, B). Preparation of parent ZnAl-LDH-NO$_3$ sample using co-precipitation method (Fig. 7A) results in formation of heterogenous aggregates of LDH sheets, which possess an extended length of ~34 nm, with poor interlayer spaces and surface properties. Existence of nitrate groups in the interlayer distance hardly compensates the positive charges in the LDH sheets affording particles with high surface charge (ζ_{av} = 16.6 mV) and conductivity. Besides, the interaction approach between the host cationic LDH sheets and the guest anions (NO$_3^-$) is exclusively driven by an electrostatic interaction, Fig. 7A. As can be seen in Fig. 7B, the microwave-assisted hydrothermal treatment employed in the synthesis of ZnAl-LDH-V$_{10}$O$_{28}$ appears to play a crucial role in facilitating the formation of various intermolecular interactions, involving electrostatic and hydrogen bond networks. The electrostatic interaction takes place between the positively charged brucite-like layers and the intercalated V$_{10}$O$_{28}^{6-}$ anions, while hydrogen bonding emanates from the interaction of the terminal V=O groups of decavanadate species with the hydroxyl groups that organized on the vertices of LDH structure and pointed to the interlayer gallery, see Fig. 7B. Such proposed interaction profile possibly causes (i) reduction in the dimensions of brucite-like layers forming LDH nanosheets of $ca.$ 6 nm length, (ii) facile exchanging of nitrate groups by interlamellar V$_{10}$O$_{28}^{6-}$ guest species, and (iii) induction of hierarchical LDH layers with a regular stacking parallel orientation. Thus, intercalation of decavanadate anions into the stacked cationic LDH nanosheets most probably develops the surface and pore characteristics of brucite-like layers linked with diminishing their zeta-potential (ζ_{av} = 8.8 mV) and conductivity measurements.

3.7. Parasiticidal activity in-vitro of ZnAl-LDH-V$_{10}$O$_{28}$ nanohybrid

Adopting a new enthusiastic step in the medication approach, the current work focuses on investigating the biological activity of the hierarchical stacked mesoporous decavanadate-intercalated LDH nanohybrid system in the field of parasitology, as this nanohybrid material is used in the treatment of foodborne and waterborne diseases which seriously threaten the global public health. Basically, this part deals with evaluating the *in vitro* parasiticidal activity of ZnAl-LDH-V$_{10}$O$_{28}$ against various developmental stages of *T. spiralis* and *S. mansoni*.

3.7.1. Cell viability assessment

It is a daunting task to assess the cell viability of ZnAl-LDH-V$_{10}$O$_{28}$ nanohybrid sample on mammalian Vero cells and estimate its corresponding IC50 values, as presented in Fig. 8a. It is acclaimed that the viability of Vero cells is relatively kept unchanged when incubated with the understudied sample at concentrations in the range 25–200 µg/ml, serving viability percentages that exceed 85% in Vero cell line. By further increasing of the concentration of ZnAl-LDH-V$_{10}$O$_{28}$ sample, the cell viability is obviously declined, recording IC50 value close to 315 µg/ml, Fig. 8a. For better understanding to the non-toxic behavior of ZnAl-LDH-V$_{10}$O$_{28}$ sample over the concentration range of 25–200 µg/ml, the photomicrographs of the control untreated Vero cells and those treated with different concentrations of the understudied nanohybrid sample are represented in Fig. 8b. It is pertinent to mention that the treated cells by ZnAl-LDH-V$_{10}$O$_{28}$ nanohybrid at dosages below 200 µg/ml seem to be well-spread and closely attached to culture substratum, resembling the regular morphology of the control untreated Vero cells, cf. Fig. 8b. At sample concentration of 200 µg/ml, the normal Vero cells begin to decay and form sparse dull spots, which are furtherly populated creating aggregates of dead cells with dark profile, see the white circles at the concentrations of 200, 300, and 350 µg/ml in Fig. 8b.

3.7.2. In vitro bioactivity evaluation of ZnAl-ldh-v10o28 nanohybrid against muscle larvae and adult worms of T. spiralis

3.7.2.1. Parasitological study. The dose-response impact and time-dependent action of ZnAl-LDH-V$_{10}$O$_{28}$ nanohybrid on the % mortality of muscle larvae and adult worms of *T. spiralis* are depicted in Fig. 9 (a, b). It is pertinent to mention that the doses of 150 and 200 µg/ml ZnAl-LDH-V$_{10}$O$_{28}$ nanohybrid seem to be significantly efficient for treatment of all the parasites (either larval or adult stages). These dosages of ZnAl-LDH-V$_{10}$O$_{28}$ possess quicker intoxication on *T. spiralis* muscle larvae than ALB drug, whereas more than 86% of ML are killed by the ZnAl-LDH-V$_{10}$O$_{28}$ concentrations of 150 and 200 µg/ml within ~17 h, i.e., the antiparasitic activity being close to 100% after 36 h of incubation. Such results most probably contradict the parasiticidal outcomes of ALB drug, which hardly records 78% mortality after 36 h exposure to ML (Fig. 9a). In addition, the parasiticidal results after 36 h exposition of *T. spiralis* adult worms with ALB drug and ZnAl-LDH-V$_{10}$O$_{28}$ (at 150 and 200 µg/ml concentrations) are comparably similar, yielding near 100% mortality, Fig. 9b. However, the kinetic curves for treatment of adult *T. spiralis* worms using ZnAl-LDH-V$_{10}$O$_{28}$ dosages of 150 and 200 µg/ml show developed % mortality values rather than those obtained by ALB drug, Fig. 9b. On the other hand, the time-response with ZnAl-LDH-V$_{10}$O$_{28}$ nanohybrid at concentrations of 75, 50, and 25 µg/ml for the treatment of *T. spiralis* ML and adult worms is markedly lower than those of ALB drug, implying the insignificant antiparasitic properties of such dosages, Fig. 9 (a, b). For the sake of convenience, the killing rates of *T. spiralis*, in percentage of parasite death per hour, with ALB drug and various doses of ZnAl-LDH-V$_{10}$O$_{28}$ nanohybrid are calculated from the slopes of their corresponding kinetic curves in the premier stages of the parasiticidal action in the range, 6–~17 h. The rates of killing parasites by ALB drug and hybrid sample are illustrated in Fig. 9c. As can be observed, the rates of parasite death (ML and/or adult worms) with ZnAl-LDH-V$_{10}$O$_{28}$ nanohybrid are markedly enhanced by increasing its doses from 25 to 200 µg/ml, Fig. 9c. It appears tempting that the killing rates of *T. spiralis* by doses of 25, 50, and 75 µg/ml ZnAl-LDH-V$_{10}$O$_{28}$ are much lower than those of ALB drug. For example, the death rates of *T. spiralis* muscle larvae and adult worms when treated by ALB drug are nearly 1.7 and 1.3 times, respectively, greater than those obtained by ZnAl-LDH-V$_{10}$O$_{28}$ at concentration of 75 µg/ml (Fig. 9c), viz, from 1.12 to 1.95% h^{-1} for ML and from 2.93 to 3.81% h^{-1} for adult worms. On contrary, treatment of ML and adult worms with higher

concentrations of ZnAl-LDH-V$_{10}$O$_{28}$ hybrid sample (150 and 200 µg/ml) afford parasite death rates higher than those recorded with ALB drug by more than 1.5-fold, e.g., from 1.95 to 3.56% h^{-1} for ML, and from 3.81 to 5.56% h^{-1} for adult worms at sample concentration of 150 µg/ml (Fig. 9c). These findings imply that ZnAl-LDH-V$_{10}$O$_{28}$ nanohybrid sample at high concentrations (150 and 200 µg/ml) displays the most potent anti-trichinella agent with fast and full intoxication on *T. spiralis* ML and adult worms at around 17 h,
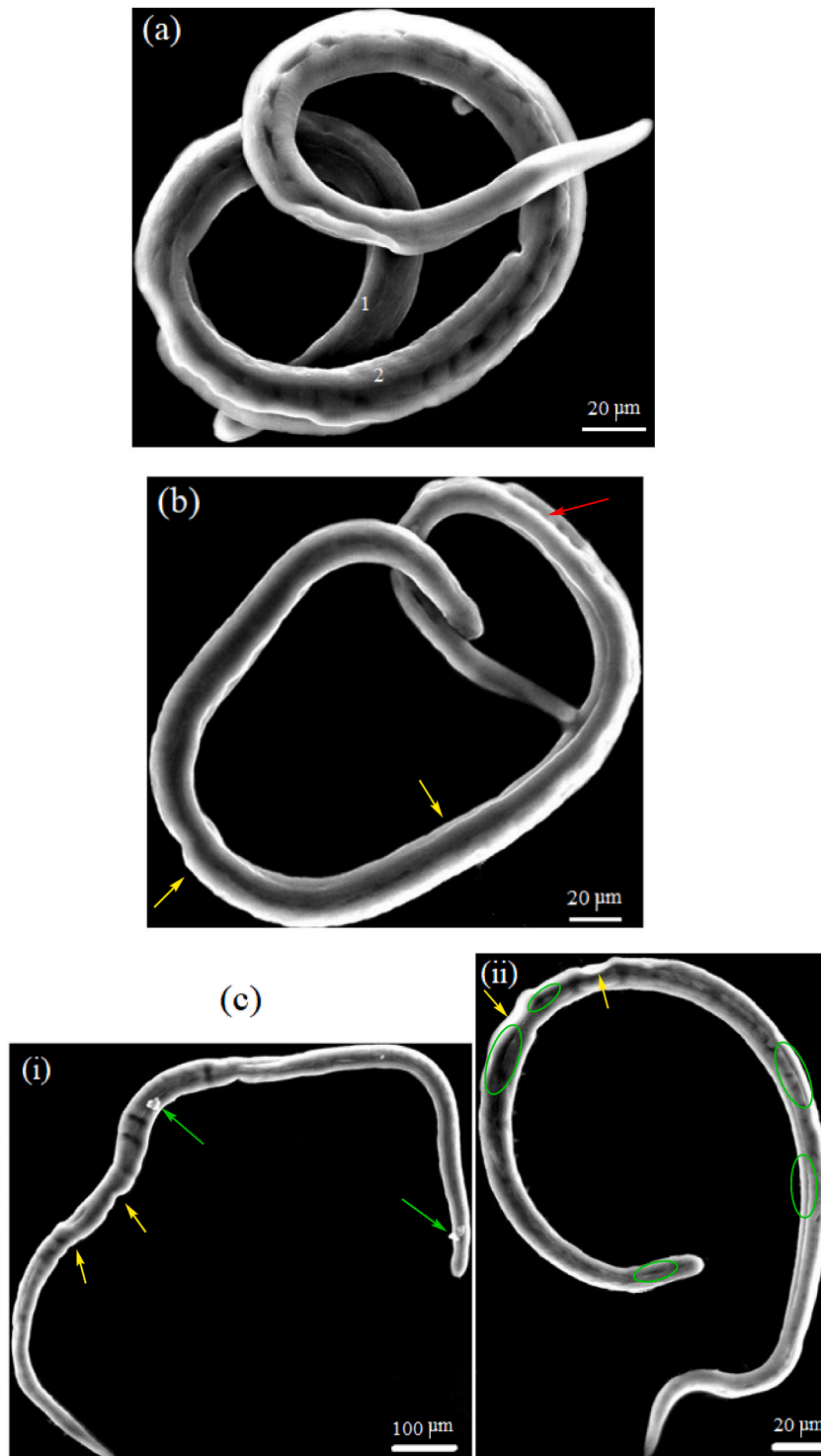
Fig. 10. SEM micrographs of: (a) control untreated *T. spiralis* muscle larvae, (b) *T. spiralis* ML treated by reference ALB drug at concentration of 30 µg/ml, and (c) *T. spiralis* ML exposed to ZnAl-LDH-V$_{10}$O$_{28}$ nanohybrid at concentration of 150 µg/ml, for 36 h incubation period.

being generally advantageous over the antiparasitic effect of reference ALB drug. Of special attention, the chosen concentrations of ZnAl-LDH-V$_{10}$O$_{28}$ nanohybrid seems also to record more developed death rates for *T. spiralis* adult worms rather than those conducted for muscle larvae, Fig. 9c. This fact may possibly reflect the accessibility of ZnAl-LDH-V$_{10}$O$_{28}$ nanohybrid particles to preferentially attack and treat *T. spiralis* adult worm with possible achievement to the hard-to-target zones in the worm body. This notion may be a sign of exhibition of ZnAl-LDH-V$_{10}$O$_{28}$ to two different parasiticidal pathways, as the violent biocidal action is monitored to kill the *T. spiralis* adult worms whilst the less aggressive one is conducted to treat the muscle larvae.

More clearness to the anti-Trichinella spiralis activity of ZnAl-LDH-V$_{10}$O$_{28}$ can be drawn from being in comparison with those of parent ZnAl-LDH-NO$_3$ sample and decavanadate orange solution (V$_{10}$O$_{28}$), Fig. 9d. It is pertinent to mention that the favourable intercalation of decavanadate anions with LDH nanosheets by the aid of microwave-assisted hydrothermal route strongly improves the biocidal performance of parent LDH layers as well as decavanadate species by more than two times (Fig. 9d).

3.7.2.2. Ultrastructural and morphological studies. To get a more sensible assessment of the diverse parasiticidal rates of ZnAl-LDH-V$_{10}$O$_{28}$ nanohybrid on *T. spiralis*, as we claimed above, the ultrastructural changes in the ML and adult worms of *T. spiralis* are investigated by SEM analysis after being treated with a nanohybrid dose of 150 μg/ml. Such dosage is highly recommended for
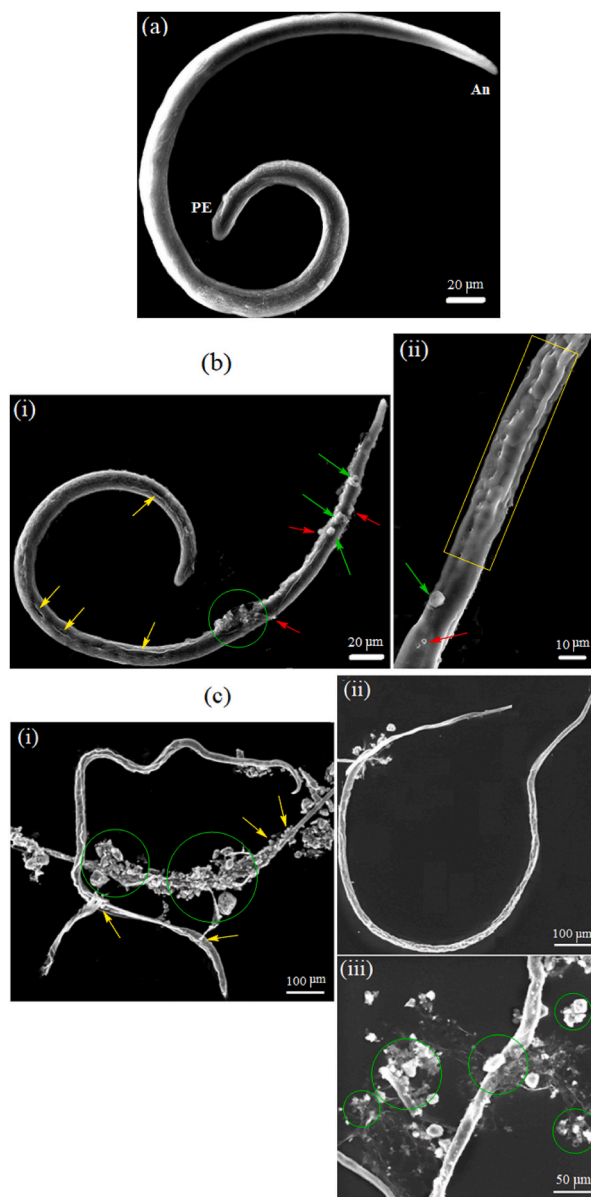
Fig. 11. SEM micrographs of: (a) control untreated *T. spiralis* adult worms, (b) *T. spiralis* adult worms treated by reference ALB drug at concentration of 30 μg/ml, and (c) *T. spiralis* adult worms exposed to ZnAl-LDH-V$_{10}$O$_{28}$ nanohybrid at concentration of 150 μg/ml, for 36 h incubation period.

treatment of parasite due to its non-toxic feature regarding to the cell viability study. For more clearness, the resultant morphology of the treated developmental stages of parasite is compared with those of the control untreated parasite and the treated one with reference ALB drug. The SEM micrographs of the control untreated muscle larvae and the treated ones are portrayed in Fig. 10(a–c). The control untreated *T. spiralis* muscle larvae (Fig. 10a) possess typical annulated cuticle morphology with defined longitudinal ridges, as represented by elements 1 and 2. Such cuticular morphology of untreated ML is kind consistent with previous work [47]. Incubation of ML with ALB drug (Fig. 10b) causes creases of cuticle (as shown by yellow arrows), remarkable flattening of the larval body, significant loss of striation, smoothening of cuticle surface, and presence of ruptured areas in the cuticle structure, as highlighted by red arrow. However, the ordinary annulations of the cuticle and the entire larval morphology are relatively still preserved, Fig. 10b. Exposition of ML to 150 μg/ml ZnAl-LDH-$V_{10}O_{28}$ nanohybrid sample yields advanced degenerative effects on the ultrastructure of muscle larvae, whereas the larval body apparently suffers thinning, stretching, and lengthening linked with significant loss of normal annulations and cuticular morphology, Fig. 10 c (i, ii). In addition, erosion of cuticle takes place with presence of numerous creases, as
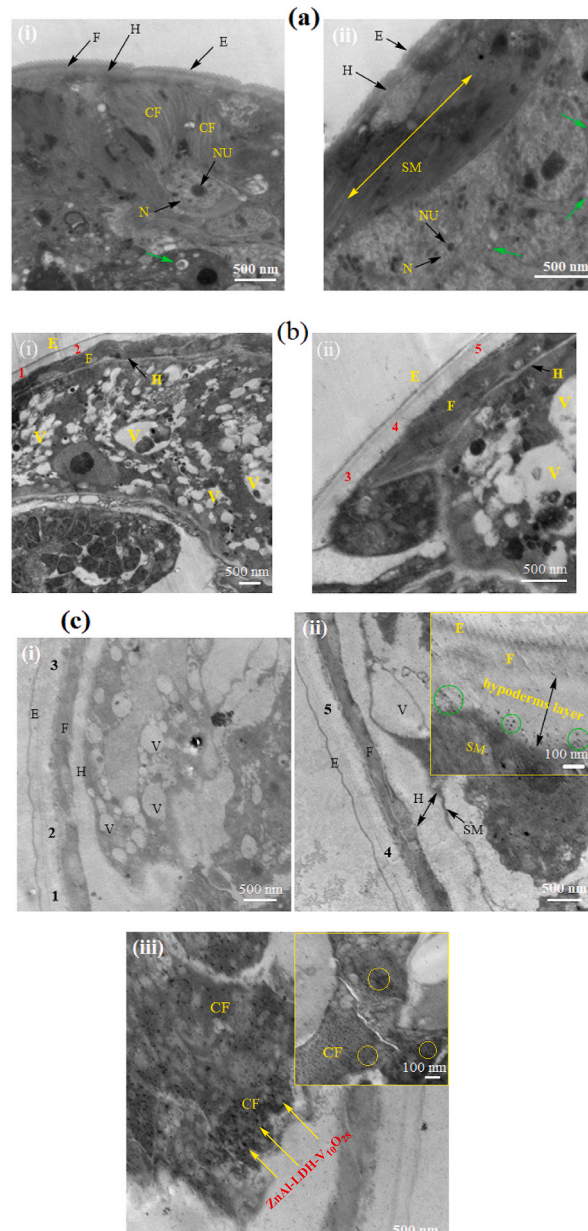
Fig. 12. TEM micrographs of: (a) control untreated *T. spiralis* adult worms, (b) *T. spiralis* adult worms treated by reference ALB drug at concentration of 30 μg/ml, and (c) *T. spiralis* adult worms combined with ZnAl-LDH-$V_{10}O_{28}$ nanohybrid at concentration of 150 μg/ml, for 36 h incubation period.

pointed by the yellow arrows in Fig. 10c (i, ii). Moreover, multiple cauliflower vesicles (see the green arrows in Fig. 10 c, i) together with populations of destructed longitudinal furrows (cf. Green circles in Fig. 10 c, ii) are plausibly appeared in the larval body. The SEM analysis of the treated adult worms of *T. spiralis* with ALB drug and 150 μg/ml ZnAl-LDH-V$_{10}$O$_{28}$ sample are performed and compared to that of control untreated parasite, see Fig. 11(a–c). By culturing *T. spiralis* adult worms in the incubation medium alone, they appear to possess primary folds with large spacing as well as normal cuticular morphology, whereas the characteristic annulations and longitudinal ridges are well-arranged onto the cuticular surface membrane associated with remarkable smoothening of cuticle in the central region of parasite body (Fig. 11a). Also, the control untreated *T. spiralis* adult worm owes attenuated anterior end (An) and thick posterior one (PE). This morphological description for *T. spiralis* adult worms is in accordance with previous literature reports [46,47]. When the *T. spiralis* adult worms incubated with ALB drug, they plausibly exhibit copious of destructed longitudinal furrows (as presented by yellow arrows in Fig. 11b, i) accompanied by abundant presence of small blebs and large vesicles (as shown by red and green arrows, respectively, in Fig. 11 b (i, ii)). Likely, fewer zones in the worm's body are greatly damaged (as represented by green circle in Fig. 11b, i), while other areas seem to suffer severe inflammation and sloughing, see the yellow rectangle in Fig. 11b, ii. Treating of adult worms of *T. spiralis* with ZnAl-LDH-V$_{10}$O$_{28}$ nanohybrid at 150 μg/ml concentration gives encouraging results, as it shows intensive lengthening and thinning of parasite body (Fig. 11c (i, ii)), complete destruction of the cuticle with presence of large blebs and significant loss of the regular annulation (as signed by yellow arrows in Fig. 11c, i), and severe erosion and fragmentation of parasite body, as shown in Fig. 11c, iii. Astonishingly, the destructed parts in the body of parasite are most probably digested and enclosed by large aggregates of ZnAl-LDH-V$_{10}$O$_{28}$ particles, as represented by green circles in Fig. 11c (i, iii), suggesting the decisive role of these particles in destroying the parasite body through being captivated by the cuticle and thence tightly interacted with the cellular structure of *T. spiralis* adult worm. By extracting the morphological changes in the treated *T. spiralis* ML and adult worms by ALB drug and ZnAl-LDH-V$_{10}$O$_{28}$ nanohybrid, it is conceivable to hypothesize that ZnAl-LDH-V$_{10}$O$_{28}$ exhibits significantly enhanced antiparasitic activity against *T. spiralis* adult worms rather than that against *T. spiralis* muscle larvae, being in concert with the parasitological results discussed in Sec. *3.7.2.1.*

To further buttress the forceful biocidal activity of ZnAl-LDH-V$_{10}$O$_{28}$ on the adult stage of *T. spiralis*, TEM investigation of the treated adult worms by ZnAl-LDH-V$_{10}$O$_{28}$ nanohybrid is carried out and compared with that conducted by ALB drug, Fig. 12. Preliminary, the TEM micrographs of the control untreated *T. spiralis* adult worms (Fig. 12a, (i, ii)) appear to save the normal morphology of the cuticle, where the cuticle structure is typical and well-defined encompassing compacted layers of epicuticle (E), fibrillar (F), and hypodermis (H). Likewise, the somatic muscles (SM) of the parasite body wall, which are attached to the underlying hypodermis layer, are supposed to be broad and well-established containing contractile filaments (CF) and many developing spheroidal mitochondria (as represented by green arrows), associated with presence of large nuclei (N) with prominent nucleolus (NU), Fig. 12 a (i, ii). These findings are quite comparable to previous work [46]. By exposition of *T. spiralis* adult worms to ALB drug (Fig. 12 b (i, ii)), the morphology of body worm is clearly degenerated, exhibiting intensive smoothening of cuticular surface membrane, remarkable divergence between epicuticle (E) and fibrillar (F) layers (as represented by elements 1–5), considerable expansion of the fibrillar layer (F) with quite contraction of the hypodermis layer (H), and marked reduction in the number of nuclei (N) and nucleolus (NU) in somatic muscles accompanied by noticeable growth in the number of vacuoles (V). On the other side, drastic morphological changes are devoted whilst treating of adult worms by ZnAl-LDH-V$_{10}$O$_{28}$ nanohybrid sample, resulting in diverse destructive progressions. At first, the epicuticle layer is severely eroded becoming much more smoothened, and the outer surface of the cuticle is obviously incurved, see Fig. 12c (i, ii). Secondly, the fibrillar layer (F) is considerably broadened and departed from the epicuticle layer (E), creating a pronounced cavitation along the interfacial region between the two layers, as represented by elements 1–5 in Fig. 12c (i, ii). The third deformation act concerns with the significant extension of the hypoderms (H) layers, where the somatic muscles are much more separated from the fibrillar layer, see Fig. 12c ii. The increased spacing between either E and F layers or F and SM layers is most probable referred to the capability of ZnAl-LDH-V$_{10}$O$_{28}$ particles to invade the outer part of the parasite and completely ruin the texture structure of the cuticle (see inset image of Fig. 12c ii), and finally accrue beyond the muscular layer, as represented by the green circles in the inset of Fig. 12c ii. At last, the somatic muscle layer is greatly damaged resulting in extensive vacuolation (Fig. 12c (i, ii)) and serious declining of contractile filaments (CF), which is vigorously attacked by ZnAl-LDH-V$_{10}$O$_{28}$ nanohybrid particles, as highlighted by yellow arrows in Fig. 12c (iii). As is also visualized in the inset image of Fig. 12c ii, the enhanced penetration ability of ZnAl-LDH-V$_{10}$O$_{28}$ particles into somatic muscles of *T. spiralis* and their fairly accumulation in the muscular layer, as signed by yellow circles, is indebted to possession of these particles to a nanolayered structure, as evidenced from XRD and TEM analysis, and a limited surface charge character, as demonstrated from zeta-potential, conductivity, and electrical impedance measurements. As is dictated by literature, the nanolayered particles of poor surface charges are considered as promising agents for cell and tissue penetration [86–88].

3.7.3. Evaluation of the in-vitro bioactivity of ZnAl-LDH-V$_{10}$O$_{28}$ nanohybrid against juvenile and adult worms of S. mansoni

3.7.3.1. Parasitological study. The impact responses of the examined dosages of ZnAl-LDH-V$_{10}$O$_{28}$ nanohybrid and their exposure time to parasite on the % mortality of juvenile and adult worms of *S. mansoni* are visualized in Fig. 13 (a, b). Running in harmony with the *in vitro* parasiticidal results during the treatment of *T. spiralis* by different dosages of ZnAl-LDH-V$_{10}$O$_{28}$ at various time intervals in the range of 6–36 h (Fig. 9 (a, b)), the ZnAl-LDH-V$_{10}$O$_{28}$ nanohybrid at concentrations of 150 and 200 μg/ml also need ~ 17 h incubation period to exterminate *S. mansoni* juvenile and adult worms, Fig. 13 (a, b). The antiparasitic activity of these nanohybrid dosages against *S. mansoni* juvenile and adult worms seems to prevail over those of reference PZQ drug, which shows about 70% effectiveness against the mortality of juvenile and adult worms after ~17 h incubation period and often achieves near 100% mortality after 36 h incubation, Fig. 13 (a, b). On contrary, exposition of *S. mansoni* juvenile and adult worms to lower concentrations of ZnAl-LDH-V$_{10}$O$_{28}$ nanohybrid
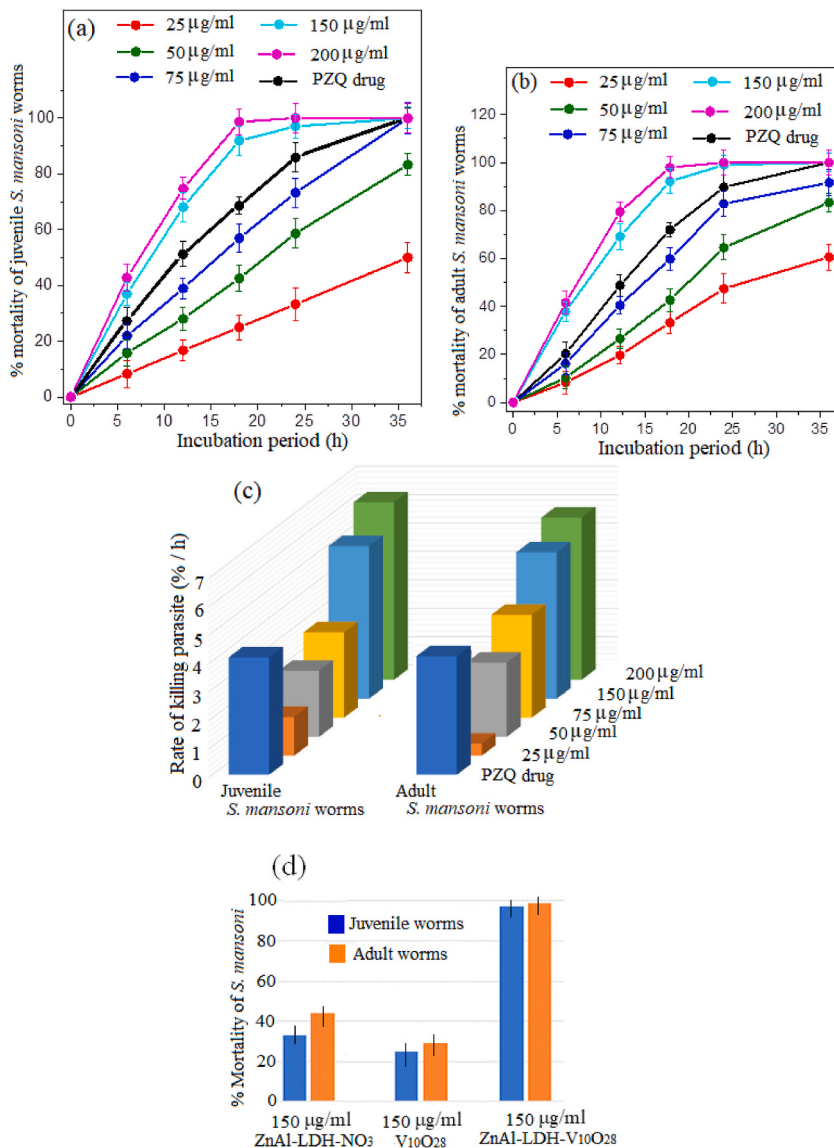
Fig. 13. Impact of time and concentration responses on the % mortality of *S. mansoni* juvenile (a) and adult (b) worms during their exposition to ZnAl-LDH-V$_{10}$O$_{28}$ nanohybrid for 36 h. Rate of killing of juvenile and adult worms of *S. mansoni* (c) using different dosages of ZnAl-LDH-V$_{10}$O$_{28}$ nanohybrid. % Mortality of *S. mansoni* juvenile and adult worms (d) using 150 μg/ml concentration of ZnAl-LDH-NO$_3$ sample and decavanadate solution (V$_{10}$O$_{28}$) in comparison to 150 μg/ml ZnAl-LDH-V$_{10}$O$_{28}$ nanohybrid sample after 36 h of incubation. For further comparison, the % mortality and the death rate of *S. mansoni* juvenile and adult stages using PZQ drug at concentration of 5 μg/ml are distinguished. Note that the bars show the range of dead worm percentages in the understudied experiments.

sample display less developed antiparasitic activity rather than those of PZQ drug, as being distinguished from the marked deterioration in the kinetic curves of the percentages of parasite death that are ranked as PZQ drug >75 μg/ml > 50 μg/ml > 25 μg/ml with respect to the used antiparasitic dosage of ZnAl-LDH-V$_{10}$O$_{28}$ nanohybrid in comparison with the reference PZQ drug, Fig. 13 (a, b). To increase the likelihood that the antiparasitic activity of ZnAl-LDH-V$_{10}$O$_{28}$ nanohybrid with 150 and 200 μg/ml concentrations is superior in treatment of various stages of *S. mansoni* compared to other understudied parasiticidal concentrations, the parasite mortality rates are calculated (following the same approach indicated for treatment of *T. spiralis*) and presented in Fig. 13 c. It can be easily envisaged that incubation of juvenile and adult *S. mansoni* worms with ZnAl-LDH-V$_{10}$O$_{28}$ at concentration of 150 μg/ml is advancing, as it yields mortality rates of about 1.3 times greater than those obtained by PZQ drug, viz., from 4.13%/h to 5.38%/h for juvenile worm, and from 3.86%/h to 5.16%/h for adult worm, Fig. 13 c. The resultant mortality rates of juvenile and adult *S. mansoni* worms caused by ZnAl-LDH-V$_{10}$O$_{28}$ with concentration of 200 μg/ml are relatively similar to those obtained with 150 μg/ml, cf. Fig. 13 c. These experimental findings most probably accentuate that the pathway of ZnAl-LDH-V$_{10}$O$_{28}$ parasiticide (at concentrations of 150 and 200 μg/ml) in the treatment of both juvenile and adult S. mansoni worms are nearly analogue, seeming unlikely to the mentioned

parasiticidal descriptions of this nanohybrid against different *T. spiralis* stages in sections *3.7.2.1. And 3.7.2.2.*

To further authenticate the advanced biocidal behavior of ZnAl-LDH-V$_{10}$O$_{28}$, the anti-schistosomal activity of such nanohybrid sample is compared to those of parent ZnAl-LDH-NO$_3$ and decavanadate solution (Fig. 13 d). It is acclaimed that intercalative hybridization of V$_{10}$O$_{28}^{6-}$ anions inside LDH nanosheets using microwave-assisted hydrothermal route significantly enthuses the % mortality of *S. mansoni* juvenile and adult worms when compared to both parent ZnAl-LDH-NO$_3$ and colored V$_{10}$O$_{28}$ solution by more than two times (Fig. 13 d), agreeing well with anti-Trichinella spiralis results.

3.7.3.2. Ultrastructural and morphological studies. To justify the resemblance in the antiparasitic action of ZnAl-LDH-V$_{10}$O$_{28}$ against juvenile and adult *S. mansoni* worms, the ultrastructural changes in the parasite body when incubated with 150 μg/ml ZnAl-LDH-V$_{10}$O$_{28}$ are recognized by SEM analysis and compared with those obtained using reference PZQ drug (Fig. 14(a–c) and 15 (a-c)). The safeness of the chosen dosage of ZnAl-LDH-V$_{10}$O$_{28}$ is highly recommended by the cell viability study (Fig. 8). As visualized in Fig. 14a, the control untreated juvenile worm displays a typical morphology with normal oral sucker (OS) and ventral sucker (VS), as shown in the inset image 1, and regular ridged teguments, as represented by white arrow in the inset image 2. In addition, a bore representing the beginning of gynaecophoric groove (GG) appears. Such acquired respective morphology complies with that reported in previous work [89]. On treating of juvenile schistosome worms with reference PZQ drug, the tegument seen along the whole worm body is
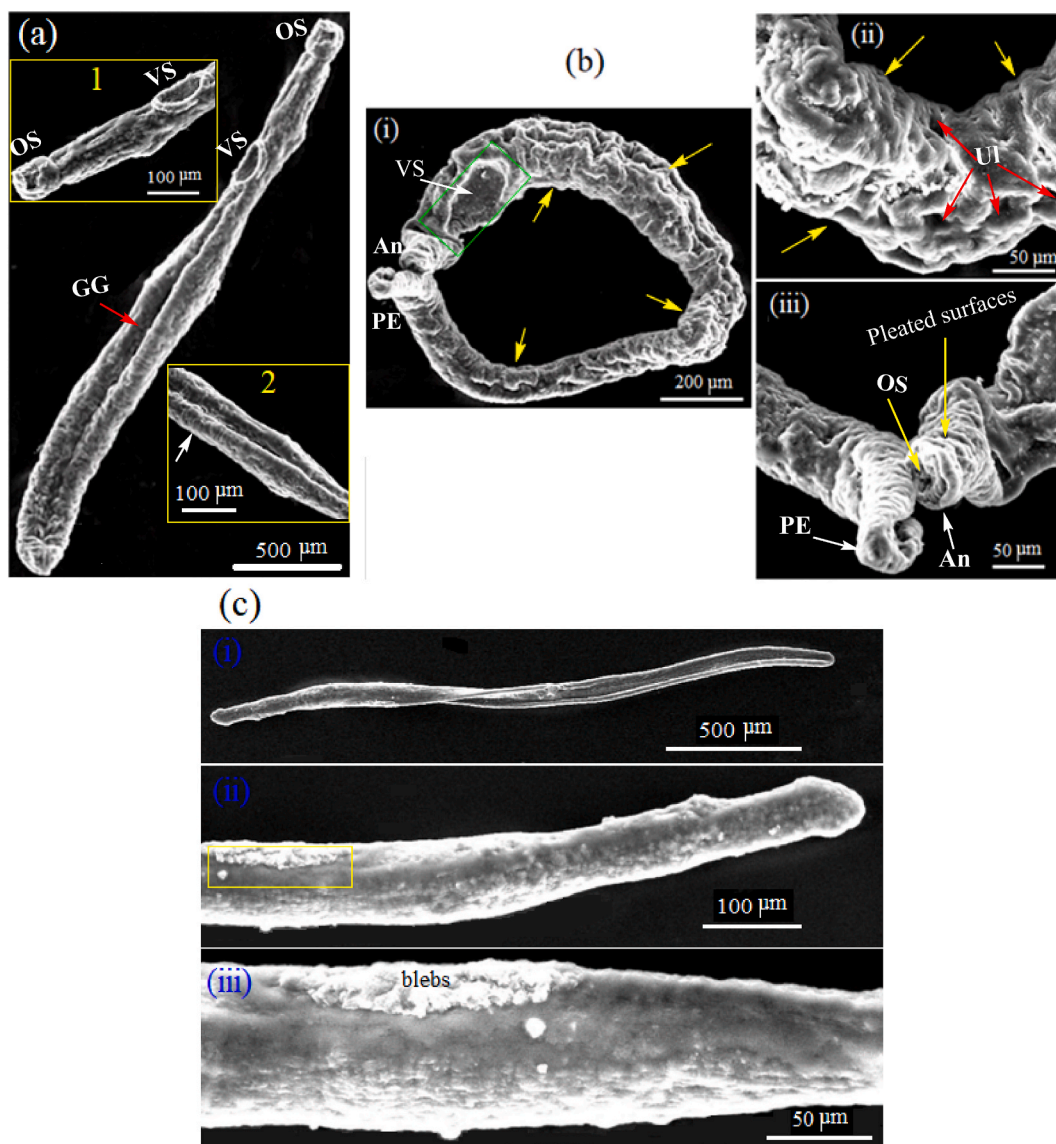
Fig. 14. SEM micrographs of: (a) control untreated *S. mansoni* juvenile worms, (b) juvenile worms of *S. mansoni* upon treatment with reference PZQ drug at concentration of 5 μg/ml, and (c) *S. mansoni* juvenile worms when exposed to ZnAl-LDH-V$_{10}$O$_{28}$ nanohybrid at concentration of 150 μg/ml, for 36 h incubation period.
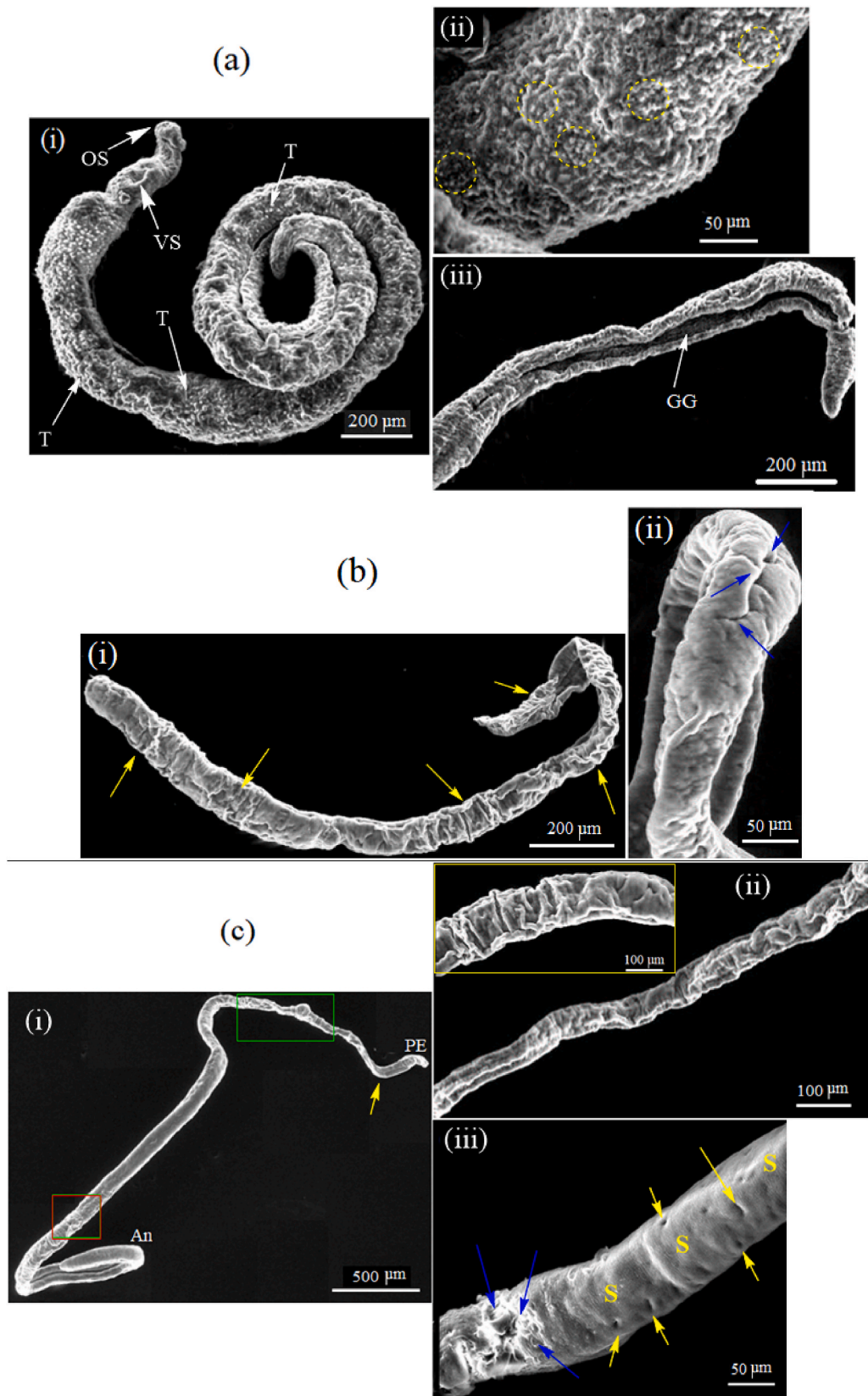
(caption on next page)

Fig. 15. SEM micrographs of: (a) control untreated *S. mansoni* adult worms, (b) adult worms of *S. mansoni* incubated with reference PZQ drug at concentration of 5 µg/ml, and (c) *S. mansoni* adult worms when treated by ZnAl-LDH-$V_{10}O_{28}$ nanohybrid at concentration of 150 µg/ml, for 36 h incubation period.

severely swelled possessing acute inflammation and surplus of creases, as highlighted by yellow arrows in Fig. 14b (i, ii), linked with significant fusion of most of the ridges and presence of extensive tegmental ulceration (Ul), see Fig. 14b, ii. Such observed weakness in the body of juvenile worm may strongly drive the anterior (An) and posterior (PE) ends of parasite to be entirely collapsed forming a ring-like shape, Fig. 14b, i. Also, the oral and ventral suckers of PZQ-treated juvenile *S. mansoni* worm are extensively swelled suffering serious deformities (see Fig. 14b, iii) with noticeable flattening of the surface of ventral sucker (as highlighted by white arrow and green rectangle in Fig. 14b, i). In addition, the oral sucker is relatively writhed, and the anterior as well as the posterior parts of worm body exhibit pleated surfaces, which are likely contiguous, cf. Fig. 14b, iii. On the other side, the juvenile *S. mansoni* worm incubated with ZnAl-LDH-$V_{10}O_{28}$ nanohybrid at concentration of 150 µg/ml exhibits a featureless morphology, as the worm body is entirely stretched, thinned, and twisted, as shown in Fig. 14c (i), and the worm tegument is subjected to severe sloughing with complete fusion of the ridges, see Fig. 14c (ii). Moreover, the oral and ventral suckers are perhaps obliterated, Fig. 14c (i). Further magnification of the contents in the yellow box in Fig. 14c (ii) reveals the abundant existence of blebs, mostly in an aggregated form, in some parts of the worm tegument, cf. Fig. 14c (iii).

Concerning the study of the morphologic alterations of adult *S. mansoni* worms when treated with reference PZQ drug and 150 µg/ ml ZnAl-LDH-$V_{10}O_{28}$, the ultrastructure of the control untreated adult schistosome worms is elucidated for comparison purposes (Fig. 15, a-c). The control untreated adult worm exhibits typical surface structure and topography, Fig. 15a (i-ii). The anterior portion of the adult worm is characterized by normal oral (OS) and ventral (VS) suckers, as shown in Fig. 15a, i. The dorsal surface of the control untreated adult *S. mansoni* worm possesses many tubercles (T) with typical spines (Fig. 15a, i). At a higher magnification of the mid-dorsal region of the untreated adult worm (Fig. 15a, ii), the tuberculate areas of the tegument presumably comprise of different shapes of papillae, as highlighted by yellow-dashed circles. Also, the surface of the adult schistosome worm exhibits a distinct and well-developed gynaecophoric groove (GG) along with parallel-arranged folds in the middle and posterior body, wherethrough mating and reproduction of worms take place (Fig. 15a, iii). The ultrastructural alterations in the adult schistosome worm treated with reference PZQ drug are given in Fig. 15b (i, ii). The PZQ drug has a significant effect on the musculature of the worms, whereas the worm body is obviously lengthened (Fig. 15b, i) linked with presence of large dorsoventral shear and bending (Fig. 15b, ii). In addition, the tubercules on the dorsal surfaces of PZQ-treated adult worm are greatly reduced or even disappeared, accompanied by marked destruction of tegumental spines, and oral and ventral suckers, cf. Fig. 15b, i. In addition, many parts of the tegument are most probably cracked with the existence of wrinkled surfaces, as presented by yellow arrows in Fig. 15b, i. As seen in Fig. 15b, ii, sloughing areas prevail along the surface of the adult worm and numerous parts of the tegument are seemingly eroded, resulting in presence of deep furrows, as represented by blue arrows.

Following the same lines of morphological alterations seen by juvenile worms when exposed to reference PZQ drug as well as ZnAl-LDH-$V_{10}O_{28}$ nanohybrid, incubation of adult *S. mansoni* worm with 150 µg/ml ZnAl-LDH-$V_{10}O_{28}$ shows much more pronounced ultrastructural changes in the parasite body rather than those distinguished from treating of adult schistosome with reference PZQ drug. As visualized in Fig. 15c (i), the parasite body treated by ZnAl-LDH-$V_{10}O_{28}$ is immensely stretched, resulting in (1) extreme thinning of the tegument, as highlighted by green rectangle, (2) remarkable contraction and curving of the anterior part (An) of the worm body, and (3) obvious writhing of the parasite body nearby the posterior portion (PE) of the adult schistosome worm, as represented by yellow arrow. Besides, tegumental eruption, and areas of cracking are also noticed along with presence of developed wrinkles and protuberance on the worm's surface (Fig. 15c, ii and its inset image). In Fig. 15c, iii, the SEM image magnifies the area in the brown box in Fig. 15c, i, adopting presence of some burst sections at the tegument with extensive lesions, as highlighted by blue arrows. Furthermore, the tegument of the incubated adult *S. mansoni* worm in the presence of ZnAl-LDH-$V_{10}O_{28}$ is intensively sloughed (S) associated with emergence of micro-erosions along the whole worm surface (as represented by yellow arrows), cf. Fig. 15c (iii).

In consideration of the above study, the destructive influence of ZnAl-LDH-$V_{10}O_{28}$ nanohybrid on the ultrastructure of juvenile and adult S. mansoni worms seem to be similar and, in turn, possibly follow a comparable parasiticidal concept, agreeing well with the parasitological data in Sec. *3.7.3.1*.

As is well known that the adult worms are the most tremendous parasitic stage in the life cycle of *Schistosoma mansoni* [90], as they colonize human blood vessels for years, and efficaciously evading the immune system while discharging thousands of eggs daily into the nearby tissues, the TEM study of the treated adult schistosome worms with ZnAl-LDH-$V_{10}O_{28}$ seems to be a vitality important issue rather than that of juvenile worms. For comparison, the TEM analysis of the control untreated and the PZQ-treated adult schistosome worm is also carried out. In the control untreated adult worm, containing of tegumental layer (TL) to numerous normal pointed spines (S) of triangular shape is evident with monitoring of well-developed muscles (M) in the subtegumental layer (STL), see Fig. 16a, (i). As viewed in Fig. 16a (ii), the tegument layer (TL) of the control untreated adult schistosome is typical and well-constructed possessing a thickness of *ca.* 0.9 µm at which the triangular-shaped spines are presumably oriented in parallel. These findings cope with previously published work [89]. Upon treatment of adult worm by reference PZQ drug (Fig. 16b, i), marked deterioration of worm tegument is noticed with remarkable loss of spines, and the thickness of TL becomes about 50% less than its original value. Furthermore, the subtegumental layer is significantly degenerated, and the worm muscles are apparently shrunk affording presence of large spaces in between (Fig. 16b, i). Magnifying view of the tegumental layer (Fig. 16b, ii) shows drastic disorganization as well as noticeable distortion of the spines, as most of them are intensively eroded losing their serrated edges to apparently form rounded spines, which prefer either to be detached from tegument, as represented by yellow arrows, or embedded into the TL, as highlighted by red circles. By
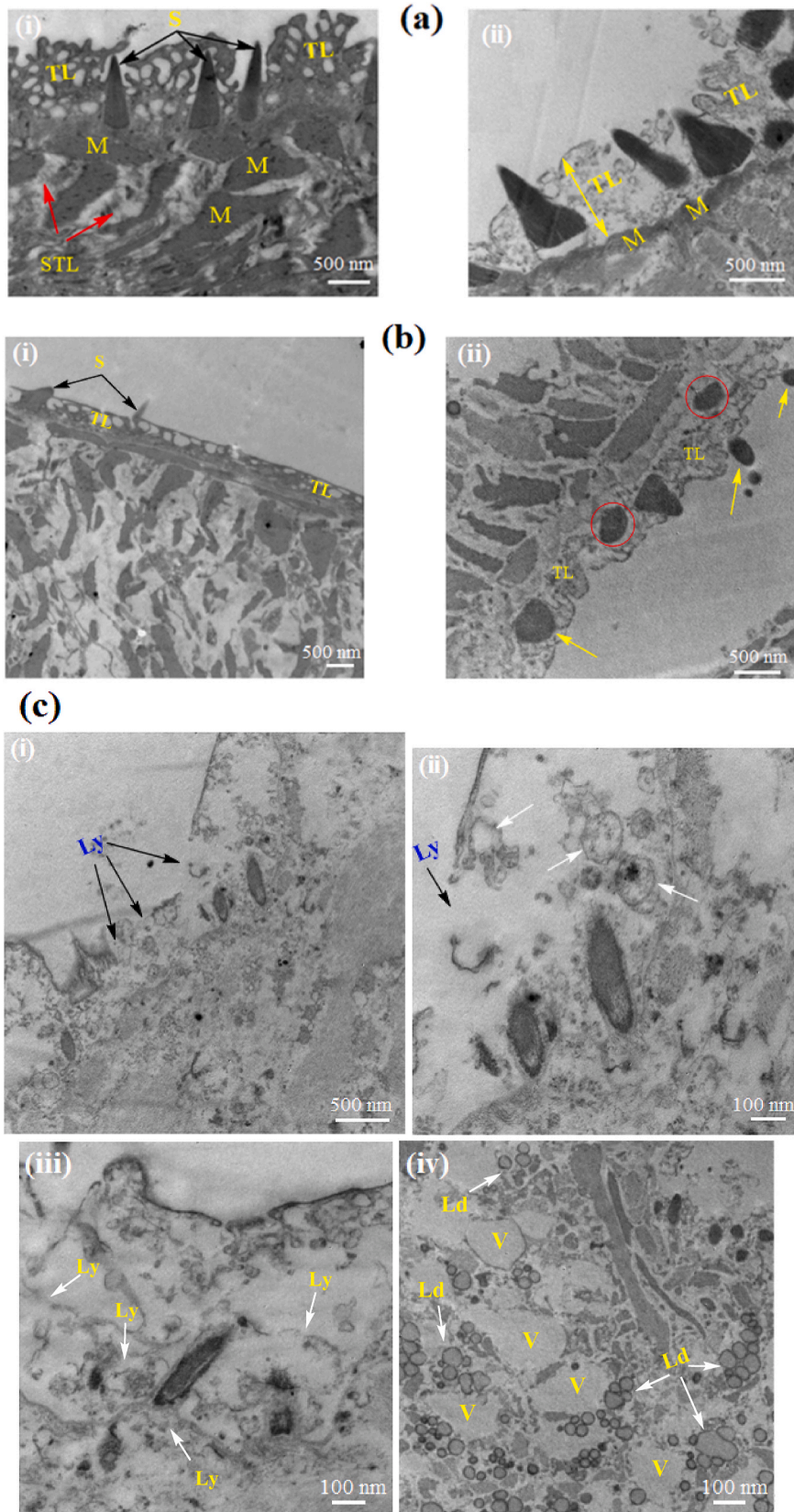
(caption on next page)

Fig. 16. TEM micrographs of: (a) control untreated *S. mansoni* adult worms, (b) *S. mansoni* adult worms treated by reference PZQ drug at concentration of 5 μg/ml, and (c) *S. mansoni* adult worms treated with ZnAl-LDH-V$_{10}$O$_{28}$ nanohybrid at concentration of 150 μg/ml, for 36 h incubation period.

incubation of adult schistosome worms with ZnAl-LDH-V$_{10}$O$_{28}$ nanohybrid, massive damage of the tegumental matrix is noted, compared to that of PZQ-treated adult worms, with appearance of focal and extensive lysis (Ly) of tegument, cf. Fig. 16c (i, ii). Besides, complete loss of spines is also seen with presence of noticeable empty sockets, as highlighted by white arrows in Fig. 16c, ii. As shown in Fig. 16 (ii, iv), the subtegumental tissues and the underlying muscle bundles in the treated adult worms assumed to be extremely demolished, affording random and featureless subtegumental structure that is significantly enriched by lysis (Ly), vacuoles (V), and lipid droplets (Ld).

3.7.4. Prospective mode of actions and pathways in the treatment of different developmental stages of T. spiralis and S. mansoni using ZnAl-LDH-V$_{10}$O$_{28}$ nanohybrid

As shown from the patterns of parasite mortality (death rate, %/h) in the different stages of *T. spiralis* and *S. mansoni* after *in vitro* treatment with 150 μg/ml ZnAl-LDH-V$_{10}$O$_{28}$ nanohybrid sample (Fig. S3, Supplementary materials), it is speculated that exhibition of
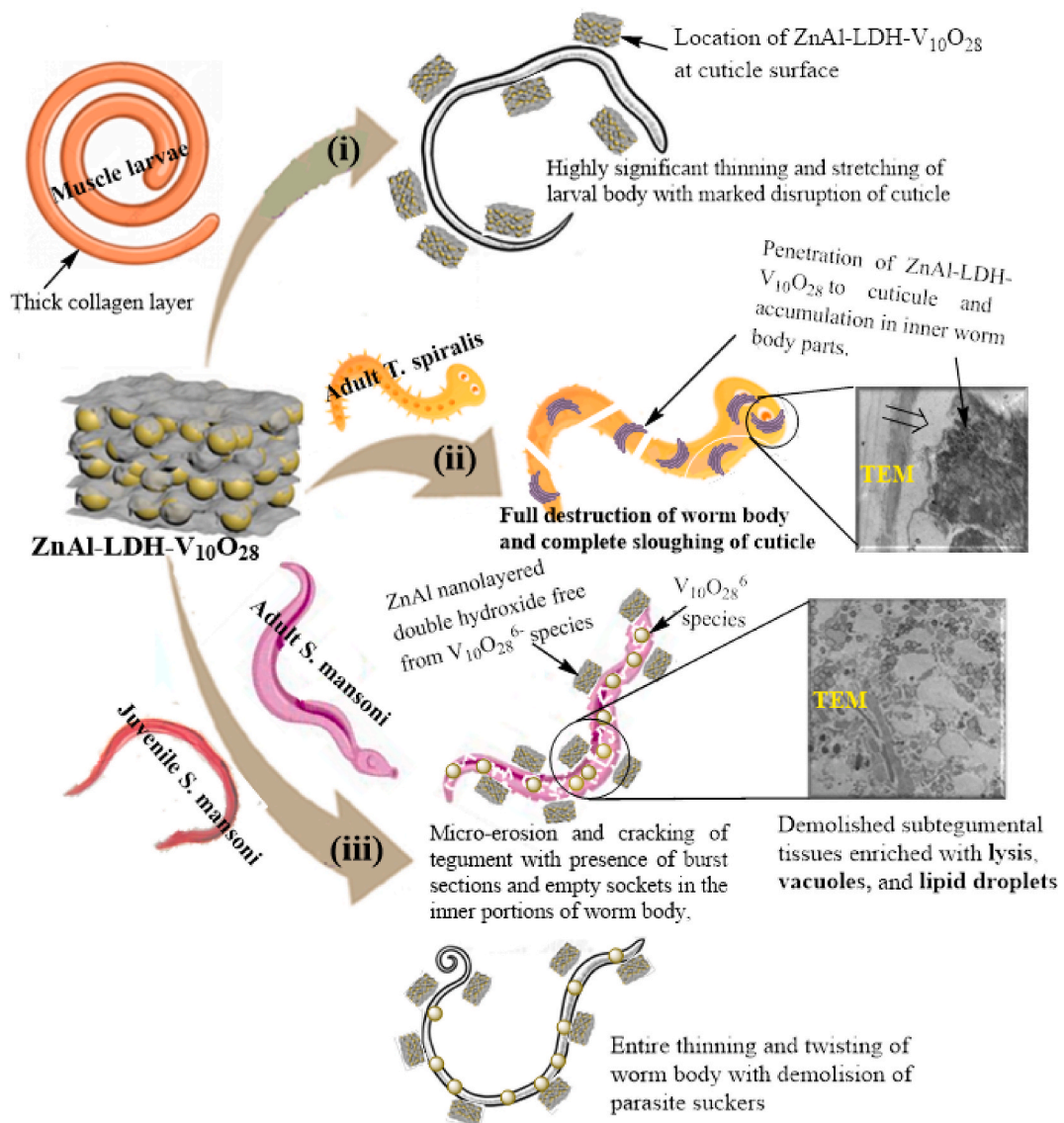
Fig. 17. Proposed parasiticidal pathways of ZnAl-LDH-V10O28 nanohybrid sample for the treatment of *T. spiralis* larval (i) and adult stages (ii), and juvenile and adult S. mansoni worms (iii), after *in vitro* exposure to ZnAl-LDH-V10O28 at concentration of 150 μg/ml for 36 h incubation period.

the treated *T. spiralis* muscle larvae and adult worms to variant response to death rate, as the killing rate of adult stage is about 1.5 times higher than that of larval one, is in marked contrast to the comparably similar killing rates given by the treated *S. mansoni* juvenile and adult worms. These outcomes may strongly reflect owing of ZnAl-LDH-$V_{10}O_{28}$ nanohybrid to diverse parasiticidal actions against the different understudied parasites stages. Another interesting remark that can be distinguished from the SEM examination of the different developmental stages of the understudied parasites (Fig. S3, Supplementary materials) is the retainment of the entire bodies of the *T. spiralis* ML, and the juvenile and adult *S. mansoni* worms when treated with ZnAl-LDH-$V_{10}O_{28}$, in spite of the extensive damages of their corresponding tegumental and subtegumental structures (as being further demonstrated from TEM investigation). Controversy, treating of *T. spiralis* adult worms by ZnAl-LDH-$V_{10}O_{28}$ shows complete destruction of the parasite body, see Fig. 11c and 12c. In view of these encouraging results, the biocidal action of ZnAl-LDH-$V_{10}O_{28}$ nanohybrid particles against *T. spiralis* adult worms is reasonably superior over the other parasiticidal approaches followed by these nanoparticles in the treatment of *T. spiralis* muscle larvae, and *S. mansoni* juvenile and adult worms.

The hypothesis of the diverse antiparasitic pathways of ZnAl-LDH-$V_{10}O_{28}$ nanohybrid can possibly arouse from two interrelated factors; (I) possession of ZnAl-LDH-$V_{10}O_{28}$ nanohybrid to near neutral particles of large electrical impedance and poor conductivity (~0.18 mS/cm) with ζ_{av} value below 9 mV, as being evidenced from the Bode diagram of impedance data (Fig. 6d) and the DLS study, and (II) exhibition of the body wall of the understudied parasites to surface membranes of variant composition and electronic nature. These perceptions may undoubtedly play a chief role in the binding affinity of ZnAl-LDH-$V_{10}O_{28}$ nanohybrid to the external body surfaces of parasites, thereby affecting its antiparasitic activity against the diverse stages of *T. spiralis* and *S. mansoni*. The prospective parasiticidal pathways of ZnAl-LDH-$V_{10}O_{28}$ nanohybrid sample for treatment of the various developmental stages of the understudied parasites are depicted in Fig. 17 (i - iii).

Along with these considerations, the muscular larvae of *T. spiralis* exhibit a specialized type of cuticle that appears as a distinct multi-layered structure of ~450 Å in thickness, representing developed resistant to digestion in the intestine of the host, evolved adaptation for encapsulation, and long survival in the muscles of the host [91,92]. This dense cuticle is mostly composed of collagen, which is conjugated with O-linked and *N*-linked glycoproteins at the cuticular surfaces of ML [92,93]. The developed thickness of the cuticular layer of ML and its hydrophilic enrichment with O-linked and *N*-linked glycans [93] most probably hinder the nearly neutral ZnAl-LDH-$V_{10}O_{28}$ nanohybrid particles to penetrate the collagen capsule of the larvae. Hence, ZnAl-LDH-$V_{10}O_{28}$ nanohybrid particles are most probably confined to occupy the surface of the larval cuticle of *T. spiralis* (Fig. 17, i), causing remarkable surface deformation in the cuticular structure of ML, as being evidenced from the SEM analysis.

On the other hand, the tegumental surface membranes of juvenile and adult *S. mansoni* worms are found to be enriched with lysophospholipids and phosphatidylcholine, as well as Na^+, K^+, Ca^{2+}, Mg^{2+} -transporting adenosine triphosphatases (ATPases), which are essential for controlling the calcium homeostasis and muscular contractility in parasite [94–97]. As the surface structure of the tegument of juvenile and adult *S. mansoni* contains plasma membrane Ca^{2+} channels [96] and integral membrane proteins with excellent hydrophilic moieties [94], reaching of the nearly neutral ZnAl-LDH-$V_{10}O_{28}$ nanohybrid particles to the inner portions of the worm body may strongly be an obstacle, where they are almost located along the tegumental tissue (Fig. 17, iii). By this way, the tegument is often the most destructive part of the treated juvenile and adult worms compared to other portions in the parasite body, dealing with SEM investigations of the various developmental stages of S. mansoni. However, the TEM analysis of the treated adult *S. mansoni* worms shows considerable damages of the inner parts of worm body. This finding perhaps attributes to the high concentrations of *P*-type ion transporting enzymes in the body of adult *S. mansoni* [95,96], fact that presumably encourages releasing of decavanadate species ($V_{10}O_{28}^{6-}$) from the interlamellar spaces of zinc aluminium LDH structure to the inner portions of worm body under possible influence of being electrostatically interacted with the ATPases enzymes in parasite (i.e., no accumulation of ZnAl-LDH-$V_{10}O_{28}$ particles is seen from the TEM image of the muscular layer of adult schistosome worm), Fig. 17 (iii). Such releasing strategy of decavanadate ions from the brucite-like layers of Zn–Al LDH is highly appreciated for corrosion inhibiting applications in previous works [29,30], but through following an anion exchange reaction of aggressive ions.

On the other hand, based on the results suggested by Milosavljevic et al. [93] and Yang et al. [98], a total of sixty-four proteins with substantial hydrophobic patches are recognized from the cuticular membranes of *T. spiralis* adult worm. Among these identified proteins, heat shock protein 70, 14-3-3 protein, and cysteine protease are of particular interest due to their (i) promising immunogenicity during infection with *T. spiralis* [98], and (ii) possession to large hydrophobic amino acid patches [98–101]. The hydrophobic domains of the cuticle surface proteins from *T. spiralis* adult worm not only facilitate binding of the nearly neutral ZnAl-LDH-$V_{10}O_{28}$ nanohybrid particles to the cuticle, but also expedite these particles to percolate through the cuticular membrane, which, in turn, cause full destruction of the muscle and subtegumental tissues of the adult *T. spiralis* worm linked with obvious accumulation of ZnAl-LDH-$V_{10}O_{28}$ nanohybrid particles deeply inside the worm body, as being highlighted from SEM and TEM studies. Such parasiticidal pathway of ZnAl-LDH-$V_{10}O_{28}$ is presented in Fig. 17, ii. Turning to the high electrical impedance of ZnAl-LDH-$V_{10}O_{28}$ nanohybrid particles, accumulation of these nanoparticles in the muscular layer of *T. spiralis* adult worm may further cause cellular starvation that finally leads to cell death [46].

Recalling the parasitological and morphological studies of ZnAl-LDH-$V_{10}O_{28}$ nanohybrid against *T. spiralis* and *S. mansoni*, the antiparasitic activity of this sample is mainly concerned with the biological properties of both Zinc aluminium LDH structure and decavanadate species. The cell adhesion affinity [102,103], the drug storage and the efficient release capability of therapeutic agents at the target sites [104,105], and biocompatibility [102,104] of the brucite-like sheets of Zn Al layered double hydroxide endows the so-synthesized nanohybrid sample by noticeable proclivity to (i) attack the cuticle of *T. spiralis* muscle larvae and the tegument surface of juvenile and adult *S. mansoni* causing marked destruction of the parasite body, cf. Fig. 10 c, 14 c, 15 c, and 16 c, and (ii) release decavanadate ions through the tegumental surface membranes of adult schistosome worm toward the subtegumental and muscle tissues of parasite, as being evidenced by TEM analysis (see Fig. 16 c), where accumulation of ZnAl-LDH-$V_{10}O_{28}$ particles in the

muscular layer of the worm are not recognized. In addition, the effective transfer of Zn Al brucite-type layers through the skin and their proficiency for cell membrane penetration [34] gives them further priority to percolate the cuticular membrane of adult *T. spiralis* worms and invade the inner body parts of parasite, as being highlighted from their corresponding SEM and TEM investigations. Furthermore, the outstanding parasiticidal performance of ZnAl-LDH-V$_{10}$O$_{28}$ against the various developmental stages of *T. spiralis* and *S. mansoni* may strongly arise from the different bioactive molecular species in the LDH sheet structure, including, (i) the oxo-bridge linkages that behave as redox catalyst in cellular destruction processes [2,103], (ii) the surface hydroxyl groups, which generate flux of •OH radicals that strongly disrupt the cell membrane [2], and (iii) Zn elements that exhibits special biological functions in the treatment of bacterial, fungal and viral infections [38,106]. Along with the antiparasitic hypothesis of zinc aluminium LDH, the binding avidity of V$_{10}$O$_{28}^{6-}$ species toward the proteins and enzymes in the undesired (tumor, parasite) cells most probable prevents the cellular oxygen consumption inducing membrane depolarization and disrupts the cell survival resulting eventually in cell death [40, 42,43]. Despite all these perceptions about the pathways of ZnAl-LDH-V$_{10}$O$_{28}$ nanohybrid sample in the treatment of varied stages of *T. spiralis* and *S. mansoni*, futuristic efforts should be paid for further in-depth studying of the molecular biology of foodborne and waterborne parasites and investigating the interactive correlations between the nanohybrid material and collagen, glycosylated proteins as well as adenosine triphosphatases in the parasite plasma membranes.

3.7.5. Comparison of parasiticidal activity of ZnAl-LDH-V$_{10}$O$_{28}$ with other biocides

For the purpose of evaluating the parasiticidal activity of ZnAl-LDH-V$_{10}$O$_{28}$ nanohybrid against *T. spiralis* and *S. mansoni*, a comparative literature survey of the recently used biocidal agents for treatment of these parasites is carried out and dedicated in supplementary materials (Fig. S4, a-c). Such comparative view is potentially indicative of the highly developed parasiticidal performance of ZnAl-LDH-V$_{10}$O$_{28}$ against either food- or water-borne parasites, where our novel nanohybrid sample seems to indispensably stand in competition with the other previously reported biocides [46,47,50,51,89,107–122] offering a near 100% biological efficiency against the different developmental stages of *T. spiralis* and *S. mansoni* within *ca.* 17 h incubation period.

4. Conclusions

The present work focuses on synthesis of hierarchically stacked (highly ordered) mesoporous ZnAl nanolayered double hydroxide (LDH) intercalated with decavanadate ions (V$_{10}$O$_{28}^{6-}$) using anion exchange process aided by microwave-assisted hydrothermal route. The physicochemical characteristics of the as-synthesized nanohybrid system (ZnAl-LDH-V$_{10}$O$_{28}$) are performed by XRD, FT-IR, Raman, XPS, SEM/EDX, HR-TEM, and N$_2$-physisorption techniques linked with DLS and conductivity studies. It can be deduced that the NO$_3^-$ ions in ZnAl layered double hydroxide structure is entirely substituted by V$_{10}$O$_{28}^{6-}$ anions, enthusing marked reduction in the crystallite size of brucite-like layers from 28 nm to ~8 nm associated with formation of well-dimensioned blocks and stacking faults for LDH sheets. Such ordered hierarchical structure results in existence of distinct interconnection of multiple LDH plates and formation of new interparticle and intragallery spaces of mesoporous structure (r̄$_h$ values in the range of ~4–40 nm). The hierarchical dense packed stacking of LDH nanosheets in ZnAl-LDH-V$_{10}$O$_{28}$ hybrid system can be emanated of the firm electrostatic interaction and hydrogen bonding between brucite-like layers and V$_{10}$O$_{28}^{6-}$ ions, fact that impose this system to exhibit particles of low zeta-potential value (~8 mV), large electrical impedance and poor conductivity (~0.18 mS/cm).

The *in vitro* antiparasitic activity of ZnAl-LDH-V$_{10}$O$_{28}$ nanohybrid system against waterborne and foodborne parasites (like *T. spiralis* and *S. mansoni*, respectively) is assessed by studying parasitological analysis and demonstrating the ultrastructural alterations in the parasite body using microscopic techniques (SEM and TEM). This system can be vitally emphasized as a potent biocidal agent for treatment of various developmental parasitic stages with near 100% mortality of parasites after about 17 h of incubation, displaying diverse parasiticidal pathways in which the biological actions of ZnAl nanolayered double hydroxide and decavanadate ions take place in an integral mode. For muscle larvae of *T. spiralis*, the ZnAl-LDH-V$_{10}$O$_{28}$ is located along the cuticle, resulting in significant thinning, and stretching of larval body with presence of numerous creases and erosions in the cuticular morphology. In the case of *T. spiralis* adult worm, the parasite body is completely ruined in consequence of the successful penetration of ZnAl-LDH-V$_{10}$O$_{28}$ nanohybrid particles to the cuticle and their accumulation in the muscle tissues. By adopting divergent biological action, the tegumental tissues of the juvenile and adult *S. mansoni* worms are invaded by ZnAl-LDH-V$_{10}$O$_{28}$, where fewer amount of V$_{10}$O$_{28}^{6-}$ species can be released from the brucite-like layers and targeted to the inner body parts of parasite. In consequence, the worm tegument is the most destructive part, as it suffers enormous sloughing, thinning, and lysing with complete elimination of spines, and oral and ventral suckers accompanied by presence of plenty of blebs, extensive lesions, micro-erosion areas, vacuoles, and lipid droplets in the inner portions of schistosome worm.

The encouraging outcomes from the *in vitro* treatment of foodborne and waterborne parasites with ZnAl-LDH-V$_{10}$O$_{28}$ nanohybrid judiciously stand it as a potential competitor to the antiparasitic action of albendazole and praziquantel drugs against trichinellosis and schistosomiasis, respectively. Such concept paves the road to a series of *in vivo* research in the ongoing future for further recognition of the biological mechanism-of-action of ZnAl-LDH-V$_{10}$O$_{28}$ on *T. spiralis* and *S. mansoni*.

Author contribution statement

Atef S. Darwish, Ph.D.: Conceived and designed the experiments; Performed the experiments; Analyzed and interpreted the data; Contributed reagents, materials, analysis tools or data; Wrote the paper.

Soheir S. Mahmoud, Ph.D.: Analyzed and interpreted the data; Contributed reagents, materials, analysis tools or data.

Fatma E.A. Bayaumy, Ph.D.: Conceived and designed the experiments; Performed the experiments; Analyzed and interpreted the

data; Contributed reagents, materials, analysis tools or data.

Data availability statement

Data will be made available on request.

Declaration of competing interest

The authors declare that they have no known competing financial interests or personal relationships that could have appeared to influence the work reported in this paper.

Appendix A. Supplementary data

Supplementary data to this article can be found online at https://doi.org/10.1016/j.heliyon.2023.e18110.

References

[1] O.O. Balayeva, A.A. Azizov, M.B. Muradov, R.M. Alosmanov, G.M. Eyvazova, S.J. Mammadyarova, Cobalt chromium-layered double hydroxide, α- and β- Co (OH)2 and amorphous Cr(OH)3: synthesis, modification and characterization, Heliyon 5 (2019), e02725.

[2] R. Sharma, G.G.C. Arizaga, A.K. Saini, P. Shandilya, Layered double hydroxide as multifunctional materials for environmental remediation: from chemical pollutants to microorganisms, Sustain. Mater. Technol. 29 (2021), e00319.

[3] J. Kim, G.H. Bak, D.Y. Yoo, Y.I. Lee, Y.G. Lee, K. Chon, Functionalization of pine sawdust biochars with Mg/Al layered double hydroxides to enhance adsorption capacity of synthetic azo dyes: adsorption mechanisms and reusability, Heliyon 9 (2023), e14142.

[4] G.H. Kang, I.K. Park, Reconstruction and intercalating anion exchange of ZnAl-layered double hydroxide, Ceram. Int. 48 (2022) 3030–3036.

[5] S. Marappa, S. Radha, P.V. Kamath, Nitrate-intercalated layered double hydroxides –structure model, order, and disorder, Eur. J. Inorg. Chem. 2013 (2013) 2122–2128.

[6] S. Megala, A. Silambarasan, S. Kanagesan, M. Selvaraj, P. Maadeswaran, R. Ramesh, M.M. Alam, M.A. Assiri, Interfacial coupling of CuWO4 nanoparticles on NiAl LDH as a novel photoctalyst for dissolved organic dye degradation, J. Mol. Struct. 1252 (2022) 132149–132160.

[7] S. Omwoma, W. Chen, R. Tsunashima, Y.F. Song, Recent advances on polyoxometalates intercalated layered double hydroxides: from synthetic approaches to functional material applications, Coord. Chem. Rev. 258 (2014) 58–71.

[8] T.T.H. Nguyen, X.T.T. Nguyen, C.Q. Nguyen, P.H. Tran, Porous metal oxides derived from Cu - Al layered double hydroxide as an efficient heterogeneous catalyst for the Friedel-Crafts alkylation of indoles with benzaldehydes under microwave irradiation, Heliyon 4 (2018), e00966.

[9] Q. Yu, H. Lei, G. Yu, X. Feng, Z. Li, Z. Wu, Influence of microwave irradiation on sludge dewaterability, Chem. Eng. J. 155 (2009) 88–93.

[10] C. Yu, Z. Cao, S. Chen, S. Wang, H. Zhong, X. Ma, In situ selenylation of molybdate ion intercalated Co-Al layered double hydrotalcite for high-performance electrocatalytic oxygen evolution reaction, J. Taiwan Inst. Chem. Eng. 119 (2021) 166–176.

[11] S.V. Sadavar, N.S. Padalkar, R.B. Shinde, S.T. Kochuveedu, U.M. Patil, A.S. Patil, R.N. Bulakhe, C.D. Lokhande, I. In, R.R. Salunkhe, J.L. Gunjakar, Mesoporous nanohybrids of 2–D Cobalt–Chromium layered double hydroxide and polyoxovanadate anions for high performance hybrid asymmetric supercapacitors, J. Power Sources 524 (2022) 231065–231077.

[12] F. Ning, M. Shao, S. Xu, Y. Fu, R. Zhang, M. Wei, D.G. Evans, X. Duan, TiO2/graphene/NiFe-layered double hydroxide nanorod array photoanodes for efficient photoelectrochemical water splitting, Energy Environ. Sci. 9 (2016) 2633–2643.

[13] K. Charradi, Z. Ahmed, P. Aranda, R. Chtourou, Silica/montmorillonite nanoarchitectures and layered double hydroxide-SPEEK based composite membranes for fuel cells applications, Appl. Clay Sci. 174 (2019) 77–85.

[14] T.D. Nguyen, A.S. Nguyen, B.A. Tran, K.O. Vu, D.L. Tran, T.T. Phan, N. Scharnagl, M.L. Zheludkevich, T.X.H. To, Molybdate intercalated hydrotalcite/ graphene oxide composite as corrosion inhibitor for carbon steel, Surf. Coat. Technol. 399 (2020) 126165–126176.

[15] J.K. Pancrecious, S.V. Vineetha, U.S. Bill, E.B. Gowd, T.P.D. Rajan, Ni-Al polyvanadate layered double hydroxide with nanoceria decoration for enhanced corrosion protection of aluminium alloy, Appl. Clay Sci. 211 (2021) 106199–106209.

[16] R. Wang, Y. Chen, Y. Liu, M. Ma, Y. Hou, X. Chen, Y. Ma, W. Huang, Synthesis of sugar gourd-like metal organic framework-derived hollow nanocages nickel molybdate@cobalt-nickel layered double hydroxide for flame retardant polyurea, J. Colloid Interface Sci. 616 (2022) 234–245.

[17] F. Kooli, W. Jones, Direct synthesis of polyoxovanadate-pillared layered double hydroxides, Inorg. Chem. 34 (1995) 6237–9238.

[18] K. Nejati, S. Davari, A. Akbari, K.A. Zeynali, Z. Rezvani, A highly active oxygen evolution electrocatalyst: Ni-Fe-layered double hydroxide intercalated with the Molybdate and Vanadate anions, Int. J. Hydrogen Energy 44 (2019) 14842–14852.

[19] Y. Cao, S. Jin, D. Zheng, C. Lin, Facile fabrication of ZnAl layered double hydroxide film co-intercalated with vanadates and laurates by one-step post modification, Colloids Interface Sci. Commun. 40 (2021) 100351–100356.

[20] G.B.B. Varadwaj, V.O. Nyamori, Layered double hydroxide- and graphene-based hierarchical nanocomposites: synthetic strategies and promising applications in energy conversion and conservation, Nano Res. 9 (2016) 3598–3621.

[21] A. Chang, T.C. Yang, M.Y. Chen, H.M. Hsiao, C.M. Yang, Hierarchical zeolites comprising orthogonally stacked bundles of zeolite nanosheets for catalytic and adsorption applications, J. Hazard Mater. 400 (2020) 123241–123249.

[22] Z. Rezvani, L.J. Foruzin, K. Nejati, Intercalation of Mordant orange 1 into ZnAl-layered double hydroxide and its dual-color photoluminescence emission, J. Mol. Struct. 1274 (2023) 134555–134561.

[23] L. Mohapatra, D. Patra, Multifunctional hybrid materials based on layered double hydroxide towards photocatalysis, in: A. Pandikumar, K. Jothivenkatachalam (Eds.), Photocatalytic Functional Materials for Environmental Remediation, John Wiley & Sons, Inc., New York, 2019, pp. 215–241.

[24] A.E. Stamate, O.D. Pavel, R. Zavoianu, I.C. Marcu, Highlights on the catalytic properties of polyoxometalate-intercalated layered double hydroxides: a Review, Catalysts 10 (2020) 57–96.

[25] K. Bahranowski, R. Dula, F. Kooli, E.M. Serwicka, ESR study of the thermal decomposition of V-containing layered double hydroxides, Colloids Surf. A Physicochem. Eng. Asp. 158 (1999) 129–136.

[26] I.D. Dobrea, C.E. Ciocan, E. Dumitriu, M.I. Popa, E. Petit, V. Hulea, Raman spectroscopy — useful tool for studying the catalysts derived from Mo and V-oxyanion-intercalated layered double hydroxides, Appl. Clay Sci. 104 (2015) 205–210.

[27] A. L Villa, D.E. de Vos, F. Verpoort, B.F. Sels, P.A. Jacobs, A study of V-pillared layered double hydroxides as catalysts for the epoxidation of terpenic unsaturated alcohols, J. Catal. 198 (2001) 223–231.

[28] M.G. Alvarez, A. Urda, V. Rives, S.R.G. Carrazan, C. Martin, D. Tichit, I.C. Marcu, Propane oxidative dehydrogenation over V-containing mixed oxides derived from decavanadate-exchanged ZnAl-layered double hydroxides prepared by a sol-gel method, C. R. Chim. 21 (2017) 210–220.

[29] M. Tabish, G. Yasin, M.J. Anjum, M.U. Malik, J. Zhao, Q. Yang, S. Manzoor, H. Murtaza, W.Q. Khan, Reviewing the current status of layered double hydroxide-based smart nanocontainers for corrosion inhibiting applications, J. Mater. Res. Technol. 10 (2021) 390–421.

[30] J. Wu, D. Peng, Y. He, X. Du, Z. Zhang, B. Zhang, X. Li, Y. Huang, In Situ formation of decavanadate-intercalated layered double hydroxide films on AA2024 and their anti-corrosive properties when combined with hybrid sol gel films, Materials 10 (2017) 426–442.

[31] M. del Arco, V. Rives, R. Trujillano, P. Malet, Thermal behaviour of Zn-Cr layered double hydroxides with hydrotalcite-like structures containing carbonate or decavanadate, J. Mater. Chem. 6 (1996) 1419–1428.

[32] F. Barahuie, M.Z. Hussein, P. Arulselvan, S. Fakurazi, Z. Zainal, Drug delivery system for an anticancer agent, chlorogenate-Zn/Al-layered double hydroxide nanohybrid synthesised using direct co-precipitation and ion exchange methods, J. Solid State Chem. 217 (2014) 31–41.

[33] R. Sahu, B.S. Mohanta, N.N. Das, Intercalation of biologically important iminodiacetatochromium(III) ion in the interlayer of ZnAl-layered double hydroxide, Indian J. Chem. 51A (2012) 812–815.

[34] S.K. Pillai, P. Kleyi, M. de Beer, P. Mudaly, Layered double hydroxides: an advanced encapsulation and delivery system for cosmetic ingredients-an overview, Appl. Clay Sci. 199 (2020) 105868–105879.

[35] M. Tomassetti, R. Pezzilli, G. Prestopino, F. Di Biagio, C. Di Natale, P.G. Medaglia, A new Clark-type layered double hydroxides-enzyme biosensor for H2O2 determination in highly diluted real matrices: milk and cosmetics, Processes 9 (2021) 1878–1890.

[36] V.K.A. Shirin, R. Sankar, A.P. Johnson, H.V. Gangadharappa, K. Pramod, Advanced drug delivery applications of layered double hydroxide, J. Contr. Release 330 (2021) 398–426.

[37] S. Bahraminejad, A. Pardakhty, I. Sharifi, A. Keyhani, E. Salarkia, M. Ranjbar, Synthesis and physicochemical characterization of Zn–Al layered double hydroxides (LDHs) as a delivery system for amphotericin B: in vitro and in silico antileishmanial study, Heliyon 9 (2023), e15308.

[38] F. Peng, D. Wang, D. Zhang, H. Cao, X. Liu, The prospect of layered double hydroxide as bone implants: a study of mechanical properties, cytocompatibility and antibacterial activity, Appl. Clay Sci. 165 (2018) 179–187.

[39] R. Ksiksi, A. Essid, S. Kouka, F. Boujelbane, M. Daoudi, N.S. Abid, M.F. Zid, Synthesis and characterization of a tetra-(benzylammonium) dihydrogen decavanadate dihydrate compound inhibiting MDA-MB-231 human breast cancer cells proliferation and migration, J. Mol. Struct. 1250 (2022) 131929–131937.

[40] E. León, V. Porro, S. Astrada, M.G. Egusquiza, C.I. Cabello, M.B. Fogolín, S.B. Etcheverry, Polyoxometalates as antitumor agents: bioactivity of a new polyoxometalate with copper on a human osteosarcoma model, Chem. Biol. Interact. 222 (2014) 87–96.

[41] X. Hu, H. Wang, B. Huang, N. Li, K. Hu, B. Wu, Z. Xiao, Y. Wei, P. Wu, A new scheme for rational design and synthesis of polyoxovanadate hybrids with high antitumor activities, J. Inorg. Biochem. 193 (2019) 130–132.

[42] M. Aureliano, C.A. Ohlin, Decavanadate in vitro and in vivo effects: facts and opinions, J. Inorg. Biochem. 137 (2014) 123–130.

[43] J.C. Pessoa, M.F.A. Santos, D. Sanna Isabel Correia, G. Sciortino, E. Garribba, Binding of vanadium ions and complexes to proteins and enzymes in aqueous solution, Coord. Chem. Rev. 449 (2021) 214192–214230.

[44] S. Pawar, M.K. Kumawat, M. Kundu, K. Kumar, Synthetic and medicinal perspective of antileishmanial agents: an overview, J. Mol. Struct. 1271 (2023) 133977–134006.

[45] K.K. Bansal, J.K. Bhardwaj, P. Saraf, V.K. Thakur, P.C. Sharma, Synthesis of thiazole clubbed pyrazole derivatives as apoptosis inducers and anti-infective agents, Mater. Today Chem. 17 (2020) 100335–100344.

[46] A.S. Darwish, M.S.A. Hussien, Z.H. Fahmy, F.E.A. Bayaumy, Lattice strain-, size-, and magnetic- dependent anti-Trichinella spiralis effect of Er3+ lightly doped zinc ferrite nanoparticles: in-vivo and in-vitro evaluations, J. Magn. Magn Mater. 545 (2022) 168744–168768.

[47] N.A. Hussien, M. Faheem, E. Sweed, A. Ibrahim, Ultrastructural tegumental changes of Trichinella spiralis adult and larval stages after in vitro exposure to Allium sativum, Exp. Parasitol. 239 (2022) 108314–108320.

[48] I. Rainova, I. Kaftandjiev, R. Harizanov, N. Tsvetkova, D. Jordanova, I. Marinova, R. Kurdova, T. Kantardjiev, N. Lalkovski, Outbreaks of human Trichinellosis, still a challenge for the public health authorities in Bulgaria, J. Publ. Health 24 (2016) 291–297.

[49] A.V. Codina, A. García, D. Leonardi, M.D. Vasconi, R.J. Di Masso, M.C. Lamas, L.I. Hinrichsen, Efficacy of albendazole: β-cyclodextrin citrate in the parenteral stage of Trichinella spiralis infection, Int. J. Biol. Macromol. 77 (2015) 203–206.

[50] S.F. Mossallam, E.I. Amer, M.H. El-Faham, Efficacy of SynriamTM, a new antimalarial combination of OZ277 and piperaquine, against different developmental stages of Schistosoma mansoni, Acta Trop. 143 (2015) 36–46.

[51] A.S. Darwish, F.E.A. Bayaumy, H.M. Ismail, Photoactivated water-disinfecting, and biological properties of Ag NPs@Sm-doped ZnO nanorods/cuttlefish bone composite: in-vitro bactericidal, cercaricidal and schistosomicidal studies, Mater. Sci. Eng. C 93 (2018) 996–1011.

[52] W.W. Duan, S. Qiu, Y. Zhao, H. Sun, C. Qiao, C. Xia, Praziquantel derivatives exhibit activity against both juvenile and adult Schistosoma japonicum, Bioorg. Med. Chem. Lett. 22 (2012) 1587–1590.

[53] E.L. Agola, I.N. Mwangi, G.M. Maina, J.M. Kinuthia, M.W. Mutuku, Transmission sites for Schistosoma haematobium and Schistosoma bovis identified in localities within the Athi River basin of Kenya using a PCR-RFLP assay, Heliyon 7 (2021), e06114.

[54] T. Elbaz, G. Esmat, Hepatic and intestinal schistosomiasis: review, J. Adv. Res. 4 (2013) 445–452.

[55] J.H. Kay, P.M. Cupit, M.C. Sanchez, G.H. Rosenberg, B. Hanelt, C. Cunningham, Transcriptional analysis of Schistosoma mansoni treated with praziquantel in vitro, Mol. Biochem. Parasitol. 186 (2012) 87–94.

[56] N.E. Nassef, I.M. Moharm, A.F. Atia, R.M. Brakat, N.M. Abou Hussien, A. Shamseldeen, Therapeutic efficacy of chitosan nanoparticles loaded with albendazole on parenteral phase of experimental trichinellosis, J. Egypt. Soc. Parasitol. 49 (2019) 301–311.

[57] Y.R. Yu, Y.F. Qi, Progress in treatment and prevention of Trichinellosis, J. Infect. Dis. Ther. 3 (2015) 1000251–1000255.

[58] Hai-yan Jiang, N. Zhao, Qiao-ling Zhang, Jiang-ming Gao, Li-li Liu, Teng-Fei Wu, Y. Wang, Qing-hua Huang, Q. Gou, W. Chen, Peng-tao Gong, Jian-hua Li, Ying-jie Gao, B. Liu, Xi-chen Zhang, Intestinal microbes influence the survival, reproduction and protein profile of Trichinella spiralis in vitro, Int. J. Parasitol. 46 (2016) 51–58.

[59] M.J. Wranicz, L. Gustowska, P. Gabryel, E. Kucharska, W. Cabaj, Trichinella spiralis: induction of the basophilic transformation of muscle cells by synchronous newborn larvae, Parasitol. Res. 84 (1998) 403–407.

[60] H. Gamble, Detection of Trichinellosis in pigs by artificial digestion and enzyme immunoassay, J. Food Protect. 59 (1996) 295–298.

[61] G.N. Leruth, G.P. Sánchez, T.L.P. Galvão, D. Boiba, S. Poznyak, J. Carneiro, J. Tedim, J.R.B. Gomes, Unveiling the local structure of 2-mercaptobenzothiazole intercalated in (Zn2Al) layered double hydroxides, Appl. Clay Sci. 198 (2020) 105842–105854.

[62] B.F. Sels, D.E. De Vos, M. Buntinx, P.A. Jacobs, Transition metal anion exchanged layered double hydroxides as a bioinspired model of vanadium bromoperoxidase, J. Catal. 216 (2003) 288–297.

[63] J. Evans, M. Pillinger, J. Zhang, Structural studies of polyoxometalate-anion-pillared layered double hydroxides, J. Chem. Soc., Dalton Trans. 14 (1996) 2963–2974.

[64] A.S. Darwish, S.K. Attia, D.I. Osman, Accelerated activation of H2O2 and persulfate by Sm-doped ZnO@highly-defective layered yttria nanocomposite under visible-light irradiation for dyeing wastewater treatment: comprehensive dominance of oxygen vacancies in photocatalytic advanced oxidation processes, J. Alloys Compd. 925 (2022) 166742–166771.

[65] K.W. Sing, D.H. Everett, R.A.W. Haul, L. Moscou, R.A. Pierotti, J. Rouquerol, T. Siemieniewska, Reporting physisorption data for gas/solid systems with special reference to the determination of surface area and porosity, Pure Appl. Chem. 57 (1985) 603–619.

[66] S.J. Gregg, K.S.W. Sing, Adsorption, Surface Area and Porosity, second ed., Academic Press, London, 1982.

[67] W. Li, A. Liu, H. Tian, D. Wang, Controlled release of nitrate and molybdate intercalated in Zn-Al-layered double hydroxide nanocontainers towards marine anticorrosion applications, Colloids Interface Sci. Commun. 24 (2018) 18–23.

[68] Z. Karami, M. Jouyandeh, J.A. Ali, M.R. Ganjali, M. Aghazadeh, S.M.R. Paran, G. Naderie, D. Puglia, M.R. Saeb, Epoxy/layered double hydroxide (LDH) nanocomposites: synthesis, characterization, and Excellent cure feature of nitrate anion intercalated Zn-Al LDH, Prog. Org. Coating 136 (2019) 105218–105223.

[69] J.P. Olivier, M. Winter, Determination of the absolute and relative extents of basal plane surface area and "non-basal plane surface" area of graphites and their impact on anode performance in lithium ion batteries, J. Power Sources 97–98 (2001) 151–155.

[70] H. Yan, J. Wang, Y. Zhang, W. Hu, Preparation and inhibition properties of molybdate intercalated ZnAlCe layered double hydroxide, J. Alloys Compd. 678 (2016) 171–178.

[71] M.Y. Ghotbi, M.Z. bin Hussein, Gallate–Zn–Al -layered double hydroxide as an intercalated compound with new controlled release formulation of anticarcinogenic agent, J. Phys. Chem. Solid. 71 (2010) 1565–1570.

[72] J.H. Olshansky, T.T. Tran, K.J. Hernandez, M. Zeller, P.S. Halasyamani, J. Schrier, A.J. Norquist, Role of hydrogen-bonding in the formation of polar achiral and nonpolar chiral vanadium selenite frameworks, Inorg. Chem. 51 (2012) 11040–11048.

[73] Z. Burghard, A. Leineweber, P.A. van Aken, T. Dufaux, M. Burghard, J. Bill, Hydrogen-bond reinforced vanadia nanofiber paper of high stiffness, Adv. Mater. 25 (2013) 2468–2473.

[74] C. Depège, L. Bigey, C. Forano, A. de Roy, J.P. Besse, Synthesis and characterization of new copper-chromium layered double hydroxides pillared with polyoxovanadates, J. Solid State Chem. 126 (1996) 314–323.

[75] H. Chai, X. Xu, Y. Lin, D.G. Evans, D. Li, Synthesis and UV absorption properties of 2,3-dihydroxynaphthale ne-6-sulfonate anion-intercalated Zn–Al layered double hydroxides, Polym, Degrad. Stab. 94 (2009) 744–749.

[76] V.S.A. Leite, B.G.L. de Jesus, V.G.O. Duartea, V.R.L. Constantino, C.M.S. Izumi, J. Tronto, F.G. Pinto, Determination of chromium (VI) by dispersive solid-phase extraction using dissolvable Zn-Al layered double hydroxide intercalated with L-Alanine as adsorbent, Microchem. J. 146 (2019) 650–657.

[77] E.L. Salinas, Y. Ono, Thermal transformation of a layered double hydroxide pillared with decavanadate isopolyanions, Bull. Chem. Soc. Jpn. 65 (1992) 2465–2470.

[78] J. Twu, P.K. Dutta, Decavanadate ion-pillared hydrotalcite: spectroscopic studies of the thermal decomposition process, J. Catal. 124 (1990) 503–510.

[79] R.B. Shinde, A.S. Patil, S.V. Sadavar, Y.M. Chitare, V.V. Magdum, N.S. Padalkar, U.M. Patil, S.T. Kochuveedu, V.G. Parale, H.H. Park, C.D. Lokhande, J. L. Gunjakar, Polyoxotungstate intercalated self-assembled nanohybrids of Zn-Cr-LDH for room temperature Cl2 sensing, Sensor. Actuator. B Chem. 352 (2022) 131046–131056.

[80] A. Barrera, F. Tzompantzi, J.C. Molin, J.E. Casillas, R.P. Hernàndez, S.U. Godinez, C. Velásquez, J.A. Alatorre, Photocatalytic activity of Ag/Al2O3 –Gd2O3 photocatalysts prepared by the sol–gel method in the degradation of 4-chlorophenol, RSC Adv. 8 (2018) 3108–3119.

[81] L. Zhang, J.S. Hu, C.L. Pan, X.H. Huang, C.M. Hou, Morphology-controllable synthesis of novel Bi25VO40 microcubes: optical properties and catalytic activities for the reduction of aromatic nitro compounds, RSC Adv. 5 (2015) 78457–78468.

[82] A. Grover, I. Mohiuddin, A.K. Malik, J.S. Aulakh, K.H. Kim, Zn-Al layered double hydroxides intercalated with surfactant: synthesis and applications for efficient removal of organic dyes, J. Clean. Prod. 240 (2019) 118090–118099.

[83] E. Alibakhshi, E. Ghasemi, M. Mahdavian, B. Ramezanzadeh, A comparative study on corrosion inhibitive effect of nitrate and phosphate intercalated Zn-Al-layered double hydroxides (LDHs) nanocontainers incorporated into a hybrid silane layer and their effect on cathodic delamination of epoxy topcoat, Corrosion Sci. 115 (2017) 159–174.

[84] Y. Guo, T. Wang, F. Chen, X. Sun, X. Li, Z. Yu, P. Wan, X. Chen, Hierarchical graphene– polyaniline nanocomposite films for high-performance flexible electronic gas sensors, Nanoscale 8 (2016) 12073–12080.

[85] A.L. Maciuca, E. Dumitriu, F. Fajula, V. Hulea, Mild oxidation of tetrahydrothiophene to sulfolane over V-, Mo- and W-containing layered double hydroxides, Appl. Catal. A-Gen. 338 (2008) 1–8.

[86] Y. Yang, S. Sunoqrot, C. Stowell, J. Ji, C.W. Lee, J.W. Kim, S.A. Khan, S. Hong, Effect of size, surface charge, and hydrophobicity of poly(amidoamine) dendrimers on their skin penetration, Biomacromolecules 13 (2012) 289–298.

[87] S.M.R. Wahba, A.S. Darwish, S.M. Kamal, Ceria-containing uncoated and coated hydroxyapatite-based galantamine nanocomposites for formidable treatment of Alzheimer's disease in ovariectomized albino-rat model, Mater. Sci. Eng. C 65 (2016) 2154–2162.

[88] S. Correa, E.C. Dreaden, L. Gu, P.T. Hammond, Engineering nanolayered particles for modular drug delivery, J. Contr. Release 240 (2016) 364–386.

[89] R.O.A. Kamel, F.E.A. Bayaumy, Ultrastructural alterations in Schistosoma mansoni juvenile and adult male worms after in vitro incubation with primaquine, Mem. Inst. Oswaldo Cruz 112 (2017) 247–254.

[90] D.G. Colley, A. L Bustinduy, W.E. Secor, C. H King, Human schistosomiasis, Lancet 383 (2014) 2253–2264.

[91] W.J. Kozek, The molting pattern in Trichinella spiralis. II. An electron microscope study, J. Parasitol. 57 (1971) 1029–1038.

[92] D.L. Lee, R.R. Shivers, A Freeze-fracture study of muscle fibres infected with Trichinella Spiralis, Tissue Cell 19 (1987) 665–671.

[93] L.S. Milosavljevic, N. Ilic, E. Pinelli, A.G. Movsesijan, Secretory products of Trichinella spiralis muscle larvae and immunomodulation: implication for autoimmune diseases, allergies, and malignancies, J. Immunol. Res. 2015 523875–523888.

[94] K. Retra, S. deWalick, M. Schmitz, M. Yazdanbakhsh, A.G.M. Tielens, J.F.H.M. Brouwers, J.J. van Hellemond, The tegumental surface membranes of Schistosoma mansoni are enriched in parasite-specific phospholipid species, Int. J. Parasitol. 45 (2015) 629–636.

[95] I.F. Abou-El-Naga, Schistosoma mansoni sarco/endoplasmic reticulum Ca2+ ATPases (SERCA): role in reduced sensitivity to praziquantel, J. Bioenerg. Biomembr. 52 (2020) 397–408.

[96] A. Da'dara, M.H. Tsai, L.F. Tao, K.A. Marx, C.B. Shoemaker, D.A. Harn, P.J. Skelly, Schistosoma mansoni: molecular characterization of a tegumental Ca-ATPase (SMA3), Exp. Parasitol. 98 (2001) 215–222.

[97] F. Noël, V.M.N. Cunha, C.L.M. Silva, D.L.M. Silva, Control of calcium homeostasis in schistosoma mansoni, Mem. Inst. Oswaldo Cruz 96 (2001) 85–88.

[98] J. Yang, W. Pan, X. Sun, X. Zhao, G. Yuan, Q. Sun, J. Huang, X. Zhu, Immunoproteomic profile of Trichinella spiralis adult worm proteins recognized by early infection sera, Parasites Vectors 8 (2015) 20–30.

[99] J.J. Caramelo, O.A. Castro, L.G. Alonso, G. de Prat-Gay, A.J. Parodi, Udp-Glc, Glycoprotein glucosyltransferase recognizes structured and solvent accessible hydrophobic patches in molten globule-like folding intermediates, Proc. Natl. Acad. Sci. U. S. A. 100 (2003) 86–91.

[100] S.A. Gillmor, C.S. Craik, R.J. Fletterick, Structural determinants of specificity in the cysteine protease cruzain, Protein Sci. 6 (1997) 1603–1611.

[101] D.H. Mohammad, M.B. Yaffe, 14-3-3 proteins, FHA domains and BRCT domains in the DNA damage response, DNA Repair 8 (2009) 1009–1017.

[102] R. Rojas, G. Mosconi, J.P. Zanin, G.A. Gil, Layered double hydroxide applications in biomedical implants, Appl, Clay Sci. 224 (2022) 106514–106528.

[103] D. Zhang, S. Cheng, J. Tan, J. Xie, Y. Zhang, S. Chen, H. Du, S. Qian, Y. Qiao, F. Peng, X. Liu, Black Mn-containing layered double hydroxide coated magnesium alloy for osteosarcoma therapy, bacteria killing, and bone regeneration, Bioact. Mater. 17 (2022) 394–405.

[104] M.A. Roch, P.A.D. Petersen, E.T. Neto, H.M. Petrilli, F. Leroux, C.T. Gueho, V.R.L. Constantino, Layered double hydroxide and sulindac coiled and scrolled nanoassemblies for storage and drug release, RSC Adv. 6 (2016) 16419–16436.

[105] A.L.M.D. De Sousa, W.M. Dos Santos, M.L. De Souza, L.C.P.B.B. Silva, A.E.H.K. Yun, C.S.B. Aguilera, B. de França Chagas, L.A. Rolim, R.M.F. da Silva, P.J. R. Neto, Layered double hydroxides as promising excipients for drug delivery purposes, Eur. J. Pharmaceut. Sci. 165 (2021) 105922–105932.

[106] H. Kabir, K. Munir, C. Wen, Y. Li, Recent research and progress of biodegradable zinc alloys and composites for biomedical applications: biomechanical and biocorrosion perspectives, Bioact. Mater. 6 (2021) 836–879.

[107] D.S. Ashour, D.M. Abou Rayia, A.E. Saad, R.H. El-Bakary, Nitazoxanide anthelmintic activity against the enteral and parenteral phases of trichinellosis in experimentally infected rats, Exp. Parasitol. 170 (2016) 28–35.

[108] F.H. Luis, A.H. Campos, R. Castillo, G.N. Vázquez, O.S. Artech, M.H. Hernández, L.Y. Mulia, Synthesis and biological activity of 2-(trifluoromethyl)-1 H -benzimidazole derivatives against some protozoa and Trichinella spiralis, Eur. J. Med. Chem. 45 (2010) 3135–3141.

[109] P.C. Sharma, D. Sharma, A. Sharma, N. Saini, R. Goyal, M. Ola, R. Chawla, V.K. Thakur, Hydrazone comprising compound s as promising anti-infective agents: chemistry and structure-property relationship, Mater. Today Chem. 18 (2020) 100349–100369.

[110] S.M. Nada, S.M. Mohammad, H.S.F. Moad, M.A. El-Shafey, A.M.F. Al-Ghandour, N. Ibrahim, Therapeutic effect of Nigella Sativa and ivermectin versus albendazole on experimental trichinellosis in mice, J. Egypt. Soc. Parasitol. 48 (2018) 85–92.

[111] R.K. Eid, D.S. Ashour, E.A. Essa, G.M. El Maghraby, M.F. Arafa, Chitosan coated nanostructured lipid carriers for enhanced in vivo efficacy of albendazole against Trichinella spiralis, Carbohydr. Polym. 232 (2020) 115826–115838.

[112] J. de Moraes, C. Nascimento, L.F. Yamaguchi, Massuo J. Kato, E. Nakano, Schistosoma mansoni: in vitro schistosomicidal activity and tegumental alterations induced by piplartine on schistosomula, Exp. Parasitol. 132 (2012) 222–227.

[113] R.N. de Oliveira, V.L.G. Rehder, A.S.S. Oliveira, V.D.L.S. Jeraldo, A.X. Linhares, S.M. Allegretti, Anthelmintic activity in vitro and in vivo of Baccharis trimera (Less) DC against immature and adult worms of Schistosoma mansoni, Exp. Parasitol. 139 (2014) 63–72.

[114] M.C. Holtfreter, M. Loebermann, S. Klammt, M. Sombetzki, P. Bodammer, D. Riebold, R. Kinzelbach, E.C. Reisinger, Schistosoma mansoni: schistosomicidal effect of mefloquine and primaquine in vitro, Exp. Parasitol. 127 (2011) 270–276.

[115] A.F. Eweas, G. Allam, A.S.A. Abuelsaad, A. Hamid Alghamdi, I.A. Maghrabi, Design, synthesis, anti-schistosomal activity and molecular docking of novel 8-hydroxyquinoline-5-sufonyl 1,4-diazepine derivatives, Bioorg. Chem. 46 (2013) 17–25.

[116] J. de Moraes, C. Nascimento, P.O.M.V. Lopes, E. Nakano, L.F. Yamaguchi, M.J. Kato, T. Kawano, Schistosoma mansoni: in vitro schistosomicidal activity of piplartine, Exp. Parasitol. 127 (2011) 357–364.

[117] S.H. Xiao, C. Qiao, J. Xue, L. Wang, Mefloquine in combination with hemin causes severe damage to adult Schistosoma japonicum in vitro, Acta Trop. 131 (2014) 71–78.

[118] J. Chen, W. Sun, J. Yang, H. Sun, Z. Wang, L. Dong, C. Qiao, C.M. Xia, Development of a novel class of pyrrolo-[1,2,5]benzothiadiazepine derivatives as potential anti-schistosomal agents, Bioorg. Med. Chem. Lett. 23 (2013) 3785–3787.

[119] N.N. Dejani, L.C. Souza, S.R.P. Oliveira, D.M. Neris, J.M.A. Rodolpho, R.O. Correia, V. Rodrigues, L.V.S. Sacramento, L.H. Faccioli, A. Afonso, F.F. Anibal, Immunological and parasitological parameters in Schistosoma mansoni-infected mice treated with crude extract from the leaves of Mentha x piperita L, Immunobiology 219 (2014) 627–632.

[120] J.K.A.L. Neves, M.D.C.A. de Lima, V.R.A. Pereira, C.M.L. de Melo, C.A. Peixoto, I.D.R. Pitta, M.C.P.A. Albuquerque, S.L. Galdino, Antischistosomal action of thioxo-imidazolidine compounds: an ultrastructural and cytotoxicity study, Exp. Parasitol. 128 (2011) 82–90.

[121] A.D.L. Aires, E.C.P.A. Ximenes, R.A.R. Silva, V.X. Barbosa, A.J.D.S. Góes, C.A. Peixoto, V.M.O. Souza, M.C.P.D.A. Albuquerque, Ultrastructural analysis of β-lapachone-induced surface membrane damage in male adult Schistosoma mansoni BH strain worms, Exp. Parasitol. 142 (2014) 83–90.

[122] F.E.A. Bayaumy, A.S. Darwish, Exfoliated Egyptian kaolin immobilized heteropolyoxotungstate nanocomposite as an innovative antischistosomal agent: in vivo and in vitro bioactive studies, Mater. Sci. Eng. C 59 (2016) 717–730.